

1 2 9 0



UNIVERSIDADE D
COIMBRA

Josué António Vermelo

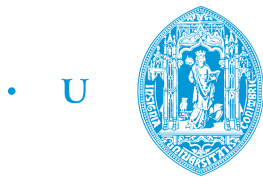
**FIRST-PRINCIPLES CALCULATION OF
SUPERCONDUCTING TRANSITION TEMPERATURE OF
 $Al_xLi_yPd_z$ TERNARY MATERIALS**

VOLUME 1

Dissertação no âmbito do mestrado em Física, ramo de Física da
Matéria Condensada, orientada pelo Professor Doutor Fernando Manuel da
Silva Nogueira e pelo Doutor Tiago Frederico Teixeira Cerqueira,
e apresentada ao departamento de Física da
Faculdade de Ciências e Tecnologia da Universidade de Coimbra.

Setembro de 2022

First-principles calculation of superconducting transition temperature of $\text{Al}_x\text{Li}_y\text{Pd}_z$ ternary materials



C •

FCTUC FACULDADE DE CIÊNCIAS
E TECNOLOGIA
UNIVERSIDADE DE COIMBRA

Josué António Vermelo
Department of Physics
University of Coimbra

A thesis submitted for the degree of
Master of Physics

September 23, 2022

Acknowledgements

I would like to thank my supervisors, Prof. Dr. Fernando Manuel da Silva Nogueira, and Dr. Tiago Frederico Teixeira Cerqueira, for their support during the elaboration of this thesis. Thanks for all.

To Dr. Pedro Miguel Castro Borlido I address my thanks for all given help, also during the elaboration of this thesis.

I would like to extend my thanks to Pe. José Luzia, Prof. Dr. Joaquim Norberto Cardoso Pires da Silva, dra. Isabel de Miranda, Instituto Universitário Justiça e Paz, Prof. Dra. Constança da Providência, and all that contributed to guarantee my financial and social stability in Coimbra and at University.

To all my colleagues at the Physics Department, particularly to Miguel Carvalho, and dr. Phinifolo Cambalame, which made these last two years more light possible.

To my parents and brothers very thanks for all the support.

Abstract

The discovery of MgB_2 's superconducting behavior spawned a new interest in conventional superconductors. One of the applications of superconductivity is in distribution of electricity over long distances. For that goal the wire must be ductile. The ductility of a superconductor material is a clear advantage in the fabrication of wires over the brittle ceramics typical of high- T_c compounds. From a theoretical point of view, there are at least two advantages of metallic superconductor materials, they have ductility, and the mechanism behind their superconductivity is known. The main goal of this thesis was to examine a set of thermodynamically stable new $\text{Al}_x\text{Li}_y\text{Pd}_z$ ternary metallic materials and determine their superconducting transition temperature from first-principles. These new materials were previously discovered by other members of the research group. We also used the density functional theory and density functional perturbation theory implemented in QUANTUM ESPRESSO software to obtain the electronic and superconducting properties. The Allen–Dynes-modified McMillan equation was applied to calculate the transition temperature. Our results show that these materials are metals and work in the weak electron-phonon coupling limit, i.e, they obey the BCS theory. The coupling constants are in the range from 0.21 to 0.33 range, while the transition temperatures are between 0 and 0.27 K.

Resumo

A descoberta do comportamento supercondutor de MgB_2 gerou um novo interesse em supercondutores convencionais. Uma das aplicações da superconductividade está na distribuição de electricidade por longas distâncias. A ductilidade de um material supercondutor é uma clara vantagem na fabricação de fios diferentemente das cerâmicas frágeis que são típicas de compostos supercondutores de alto T_c . Do ponto de vista teórico, existem pelo menos duas vantagens dos materiais supercondutores metálicos, eles têm ductilidade e o mecanismo por detrás de sua superconductividade é conhecido. O objetivo principal desta tese foi analisar um conjunto de novos materiais metálicos ternários $\text{Al}_x\text{Li}_y\text{Pd}_z$ termodinamicamente estáveis e determinar sua temperatura de transição supercondutora a partir dos primeiros princípios. Os novos materiais foram previamente previstos por outros membros do grupo de investigação. Usamos a teoria do funcional de densidade e teoria perturbativa do funcional de densidade implementadas no software QUANTUM ESPRESSO para obter as informações electrónicas e supercondutoras. A equação de McMillan modificada por Allen-Dynes foi aplicada para calcular a temperatura de transição. Nossos resultados mostram que esses materiais são metais e funcionam no limite fraco de acoplamento electrão-fonão, ou seja, obedecem à teoria BCS. As constantes de acoplamento estão na faixa de 0,21 a 0,33, enquanto as temperaturas de transição estão entre 0 e 0,27 K.

Contents

1	Introduction	1
2	Many-body problem, DFT and DFPT	3
2.1	Introduction	3
2.1.1	Approximate solutions of the many-body Schrodinger's equation	4
2.2	Density functional theory	6
2.2.1	The Kohn-Sham approach	8
2.2.2	Local density approximation	9
2.3	Self-consistency	10
2.4	Density functional perturbation theory	11
2.4.1	The lattice vibrations and electronic structure theory	11
2.4.2	Hellmann-Feynman theorem	12
2.4.3	Linear response	13
2.5	Pseudopotential Approximation	14
2.5.1	Norm conserving pseudopotential	16
3	Superconductivity	18
3.1	Periodic solids and electronic bands	18
3.1.1	Fundamental types of three-dimensional lattices	19
3.1.2	The reciprocal lattice and Brillouin zone	20
3.1.3	Bloch's theorem	21
3.1.4	Band structure and density of states	22
3.1.5	Integrals in \mathbf{k} -space and special \mathbf{k} -points	22
3.2	Lattice vibrations and phonons	23
3.2.1	One-dimensional diatomic lattice	23
3.2.2	General case	25
3.2.3	Phonons	25
3.3	Superconductivity	26
3.3.1	Cooper pairs and BCS theory	26
3.3.2	Eliashberg theory and McMillan-Allen-Dynes formula for T_c	28
4	Methodology	30
5	Results	37
5.1	Electronic structure calculations	37
5.2	Phonon spectra and T_c calculations	40
5.2.1	Phonon spectra and T_c of the hexagonal structures	40

5.2.2	Phonon spectra and Tc of the fcc structures	44
5.2.3	Phonon spectra and Tc of the Trigonal R (3 fold axis c) structures	48
5.2.4	Summary	50
6	Conclusions	51
A A.	The 230 crystallographic space groups	52

List of Figures

2.1	Schematic representation of the self-consistent loop.	11
2.2	Model of a solid and valence electrons using ionic cores [1].	14
2.3	Schematic representation of the construction of the pseudo-wavefunction ϕ and pseudopotential V^{ps} [2].	15
3.1	Primitive (A and B) and non-primitive (C and D) 2D unit cells [3]. . .	19
3.2	Construction of Wigner-Seitz cell (the hexagon inscribed by the dashed lines)[4].	19
3.3	The fourteen Bravais lattices in three dimensions [5].	20
3.4	Brillouin zone and high symmetry path for FCC, on the left, and Hexagonal, on the right, structures with $b_1 \equiv a^*$, $b_2 \equiv b^*$, $b_3 \equiv c^*$ (adapted from [6]).	21
3.5	Simple diatomic chain model, with atoms of different mass connected by harmonic forces that are of equal strength between all nearest-neighbour atom pairs[7].	24
3.6	Dispersion curve of the diatomic chain model[8][7].	25
3.7	Electron-electron interaction mediated by phonon (adapted from [9]). .	27
4.1	Cutoff convergence for MgB_2	32
4.2	Hexagonal structure of MgB_2 . left: primitive unit cell; right: 2x2 super-cell viewed from the z direction. Images obtained using xcrystden[10]. .	33
4.3	High-symmetry path, $\Gamma-M-K-\Gamma-A-L-H-A$, for hexagonal structure in xcrystden [10].	33
4.4	Electronic structure and DOS of MgB_2	34
4.5	Phonon spectrum, on the left, and phonon DOS, on the right, of MgB_2 for 12x12x12 k-point grids, 6x6x6 q-point grids and $n_k = 16$. Particularly, in the phonon DOS the black graph is the total DOS, the green is the contribution of Mg and the dark-orange are the B contributions. . .	35
4.6	Coupling constant of MgB_2 as a function of the smearing parameter. . .	36
4.7	Transition temperature of MgB_2 as a function of the smearing parameter. 36	36
5.1	Hexagonal structure of $\text{Al}_2\text{Li}_2\text{Pd}_2$. Left: primitive unit cell; right: z direction visual with 2 unit cells in the x and y directions.	38
5.2	Hexagonal structure of $\text{Al}_2\text{Li}_3\text{Pd}$. Left: primitive unit cell; right: z direction visual with 2 unit cells in the x and y directions.	38
5.3	Hexagonal structure of Al_3LiPd_2 . Left: primitive unit cell; right: z direction visual with 2 unit cells in the x and y directions.	38

5.4	Hexagonal structure of AlLi_2Pd_3 . Left: primitive unit cell; right: z direction visual with 2 unit cells in the x and y directions.	39
5.5	Hexagonal structure of AlLi_4Pd . Left: primitive unit cell; right: z direction visual with 2 unit cells in the x and y directions.	39
5.6	fcc structure of Al_2LiPd . Left: primitive unit cell; right: z direction visual with 2 unit cells in the x and y directions.	39
5.7	fcc structure of AlLiPd_2 . Left: primitive unit cell; right: z direction visual with 2 unit cells in the x and y directions.	40
5.8	Trigonal structure of Al_4LiPd (leftmost figures) and $\text{Al}_2\text{Li}_2\text{Pd}$ (rightmost figures). First and third figures: primitive unit cells; second and fourth figures: z direction visual with 2 unit cells in the x and y directions. . .	40
5.9	Electronic band structure and DOS of $\text{Al}_2\text{Li}_2\text{Pd}_2$	41
5.10	Electronic band structure and DOS of $\text{Al}_2\text{Li}_3\text{Pd}$	41
5.11	Electronic band structure and DOS of Al_3LiPd_2	42
5.12	Electronic band structure and DOS of AlLi_2Pd_3	42
5.13	Electronic band structure and DOS of AlLi_4Pd	43
5.14	Electronic band structure and DOS of Al_2LiPd	43
5.15	Electronic band structure and DOS of AlLiPd_2	44
5.16	Electronic band structure and DOS of Al_4LiPd	44
5.17	Electronic band structure and DOS of $\text{Al}_2\text{Li}_2\text{Pd}$	45
5.18	Phonon spectrum and density of states of phonon of Al_3LiPd_2 , with blue color for Pd contribution, yellow and green for Al contribution, and finally, red color for Li contribution.	45
5.19	Phonon spectrum and density of states of phonon of AlLi_2Pd_3 , with yellow and orange for Pd contribution, green for Al, and finally, red color for Li contribution.	46
5.20	Phonon spectrum and density of states of phonon of $\text{Al}_2\text{Li}_3\text{Pd}$, with yellow color for Pd contribution, red for Al contribution, and finally, blue color for Li contribution.	46
5.21	Phonon spectrum and density of states of phonon of AlLi_4Pd , with blue color for Pd contribution, dark blue for Al contribution, and finally, other colors for Li contribution.	47
5.22	Phonon spectrum and density of states of phonon of $\text{Al}_2\text{Li}_2\text{Pd}_2$, with red color for Pd contribution, yellow and orange for Al contribution, and finally, blue color for Li contribution.	47
5.23	Phonon spectrum and density of states of phonon of Al_2LiPd , with orange color for Pd contribution, blue for Al contribution, and finally, yellow color for Li contribution.	48
5.24	Phonon spectrum and density of states of phonon of AlLiPd_2 , with orange color for Pd contribution, blue for Al contribution, and finally, yellow color for Li contribution.	48
5.25	Phonon spectrum and density of states of phonon of $\text{Al}_2\text{Li}_2\text{Pd}$, with green color for Pd contribution, grey for Al contribution, and finally, blue color for Li contribution.	49

5.26 Phonon spectrum and density of states of phonon of Al₄LiPd, with red color for Pd contribution, blue, yellow and grey for Al contribution, and finally, green color for Li contribution. 49

List of Tables

3.1	Selected superconductors (adapted from [11]).	26
4.1	Frequency, in cm^{-1} , of the phonon modes of MgB2 at Γ point for k-point grids (k, k, k) with $k = 12$, $k = 15$ and $k = 16$, from left to the right. . .	34
5.1	Resume of the crystalline information of the $\text{Al}_x\text{Li}_y\text{Pd}_z$ ternary materials.	37
5.2	Summary of the Tc calculations for the $\text{Al}_x\text{Li}_y\text{Pd}_z$ ternary materials. . .	50
A.1	The 230 Crystallographic Space Groups (adapted from [12])	52

Chapter 1

Introduction

The discovery of the superconducting state in mercury, in 1911, by Kamerlingh Onnes opened a new scientific area that remains technologically and scientifically promising. More than one hundred years later, this area is still dynamic and rich, always manifesting novel properties or phenomena.

Although there are superconductors with significantly high transition temperature (T_c), see section 3.3, such as the high-temperature superconducting cuprates, these materials are highly anisotropic and inherently brittle, factors that constitute serious handicaps and challenges for their technological applications as conductor wires and tapes for transmission cables and high-field electromagnets [13].

Different from the conventional superconductors (which obey the BCS theory 3.3.1), another handicap for these high- T_c cuprates and pnictides superconductors is the unknown mechanism behind their superconductivity.

With respectively a $T_c = 15$ K and $T_c = 18.5$ K for NbTi and Nb₃Sn conventional superconductors, these materials are used to generate high magnetic fields between 10 - 20 T. The first one, with critical magnetic field¹ (H_c) equal to 15 T, is an alloy with low efficiency. The second one is intermetallic and is more efficient, with $H_c = 30$ T. However, the last one is difficult to fabricate and, therefore, more expensive.

For long distances, it is necessary to have not only a high- H_c superconductor but also to be accessible and malleable. These characteristics are useful for long distances electricity distribution and fabrication of coil windings, technologies of high importance.

Generally, metallic materials present the last property (malleability). That means that a metallic superconductor with T_c around 20 K, H_c about 30 T, and easy to fabricate could be feasible for long power transmission cables production. Thus, the transmission of large quantities of power to densely populated regions could be possible, helping with health, safety, and environmental problems.

The above information is sufficient to motivate searching metallic superconductor materials to find at least one with all the above-listed properties.

Nowadays, it's possible to predict materials' properties using materials' quantum simulations. For that goal, there are theoretical and computational methods with different complexities.

¹While small magnetic fields are expelled from the interior of a superconductor material, there exists a limit magnetic field which destroys the superconductivity of the material. This limit magnetic field is the so-called critical magnetic field (H_c)

The most used approaches for modern quantum simulations of crystalline materials are the density functional theory (DFT) used to predict ground state properties such as the crystalline structure, electronic band structure, etc, and the density functional perturbation theory (DFPT) used to predict the lattice vibrations' related properties such as phonon spectra.

DFT and DFPT have great applicability in modern studies of many-body systems due to their affordable computational effort [14], and their accuracy in predicting the properties of the materials giving a quantitative understanding of these properties [15][16], including all quantum effects of the many-body systems (exchange and correlation effects) in their structure, although by approximations.

The rudimentary exchange-correlation functional energy is the local density approximation (LDA). But this approximation has acceptable accuracy for electronic and phonon calculations for metallic materials. Thus, we hope to use this approximation to predict the electronic properties (crystalline structure, lattice parameters, electronic band structure, and density of states), phonon spectrum, coupling constant, and superconducting transition temperature of a set of new ternary material with Aluminum, Palladium, and Lithium elements in different combinations.

The structure of this thesis is the following: in the second and third chapters, we present topics about DFT, DFPT, and solid-state and superconductivity concepts. With this background, we proceed in chapter four with the methodology, where we present the steps of the computational calculus and show the results of magnesium diboride (MgB_2). In the final chapter, fifth, we present the results of the new ternary materials and conclusions. We also present in the last chapter what is possible to do as the next step of study of these materials.

Chapter 2

Many-body problem, DFT and DFPT

2.1 Introduction

All matter is a collection of atoms. To be more precise, a collection of nuclei and electrons.

Materials hold together owing to a balance between the repulsive Coulomb interactions of pairs of electrons and nuclei, and the attractive Coulomb interactions between electrons and nuclei [17].

In quantum theory, to study any non-relativistic quantum system (which will remain the domain of our work), we must solve the Schrödinger equation associated, i.e, for any non-relativistic material, we must solve an equation with the following Hamiltonian in atomic units ¹:

$$\hat{H} = - \sum_i \frac{1}{2} \nabla_i^2 - \sum_I \frac{1}{2M_I} \nabla_I^2 + \sum_{i < j} \frac{1}{|\mathbf{r}_i - \mathbf{r}_j|} + \sum_{I < J} \frac{Z_I Z_J}{|\mathbf{R}_I - \mathbf{R}_J|} - \sum_{i, I} \frac{Z_I}{|\mathbf{R}_I - \mathbf{r}_i|} \quad (2.1)$$

or,

$$\hat{H} = \hat{T}_e + \hat{T}_n + \hat{V}_{\text{int}} + \hat{E}_{\text{nn}} + \hat{V}_{\text{ext}} \quad (2.2)$$

In equation (2.1), \mathbf{r}_i , \mathbf{R}_I , M_I , and Z_J are the electronic degrees of freedom, the nuclear degrees of freedom, the I^{th} nucleus mass, and the J^{th} nucleus charge, respectively [18]. In equation (2.2), \hat{T}_e is the electronic kinetic energy, \hat{T}_n is the nuclei kinetic energy, \hat{V}_{int} is the potential energy of electron-electron interaction, \hat{E}_{nn} is the potential energy of nucleus-nucleus interaction, and, \hat{V}_{ext} is the potential energy of electron-nucleus interaction. Small case indices indicate electronic degrees of freedom, upper case indicates the nuclear coordinates.

A system described by this equation has nuclei and electrons moving and interacting relatively to and with each other. Thus, we must solve a many-body Schrödinger's equation.

Solving the many-body Schrödinger's equation is one of the grand challenges of theoretical physics: to develop theoretical approaches and computational methods that

¹In atomic units we have $\hbar = e = m_e = \frac{1}{4\pi\epsilon_0} = 1$

can accurately treat the interacting system of many electrons and nuclei[19], particularly for solids that are our object in this thesis.

2.1.1 Approximate solutions of the many-body Schrodinger's equation

Born–Oppenheimer approximation

As said above, the Schrodinger equation with the Hamiltonian in 2.1 is difficult, indeed impossible, to solve, even analytically. However, the nuclei masses are higher than the masses of the electrons. This masses difference is reflected in the higher motion of electrons relative to the nuclei motion. That means the electronic energies are higher than nuclei energies, and the electrons adapt quickly to any change in nuclei positions. Therefore, we can determine the electronic motion for each fixed nuclei position.

These arguments make it possible to think that we can separate the problem in electronic and nuclear terms, where the electronic issue satisfies the following Schrodinger equation

$$\hat{H}_e \Psi_{\mathbf{R}}^l(\{\mathbf{r}_i\}) = \left[\hat{T}_e + \hat{V}_{\text{int}} + \hat{V}_{\text{ext}} \right] \Psi_{\mathbf{R}}^l(\{\mathbf{r}_i\}) = E^l(\{\mathbf{R}_I\}) \Psi_{\mathbf{R}}^l(\{\mathbf{r}_i\}) \quad (2.3)$$

with the electronic wavefunction depending parametrically on the nuclei position. $E^l(\{\mathbf{R}_I\})$ is the l^{th} eigenvalue of the electronic subsystem for a given set of nuclear coordinates.

Thus, the full wavefunction can be written as a sum of products of nuclear and electron wavefunctions, $\Phi^l(\{\mathbf{R}_I\})$ and $\Psi_{\mathbf{R}}^l(\{\mathbf{r}_i\})$, i.e. $\chi(\{\mathbf{r}_i\}; \{\mathbf{R}_I\}) = \sum_l \Psi_{\mathbf{R}}^l(\{\mathbf{r}_i\}) \Phi^l(\{\mathbf{R}_I\})$. When we act the Hamiltonian in 2.2 in $\chi(\{\mathbf{r}_i\}; \{\mathbf{R}_I\})$, multiply by $\Psi_{\mathbf{R}}^{k*}(\{\mathbf{r}_i\})$ and integrate by \mathbf{r} we get the nuclear problem, where nuclear motion is realised in an electronic potential $E^l(\{\mathbf{R}_I\})$.

The parametric dependence of the electron wavefunction in the nuclei position originates two extra terms, in the nuclear problem, that are proportional to the inverse mass of the nuclei and, one, the first and, another one, second variations of the electronic wavefunction due to the nuclei position changes ($\nabla_{\mathbf{R}} \Psi_{\mathbf{R}}^{k*}(\{\mathbf{r}_i\})$ and $\nabla_{\mathbf{R}}^2 \Psi_{\mathbf{R}}^{k*}(\{\mathbf{r}_i\})$). We can neglect these two extra terms and get the Born-Oppenheimer approximation.

Actually, in this approximation, after solving the electronic problem, we introduce the nuclear motion as a perturbation, and both subsystems, electronic and nuclear, contribute to the materials' properties.

The spin can easily be included in the formalism if we specify each particle's coordinates as $(\mathbf{r}_i, \sigma_i) \equiv \mathbf{x}_i$

Independent electrons

In the Born–Oppenheimer approximation, the next question is how can we write the solution for the electronic Schrodinger equation, which is still a tricky problem.

The next step is reducing the difficulty considering that the electrons don't feel the other electrons, and then we can remove the V_{int} from the Hamiltonian. This new approximation is called the independent electrons approximation and has

$$\hat{H}_e = \hat{T}_e + \hat{V}_{\text{ext}} \quad (2.4)$$

and a solution for the independent electrons Schrodinger's equation can be written as a product of each independent electron's wavefunctions, $\phi_i(\mathbf{x}_i)$:

$$\Psi(\mathbf{x}_1, \mathbf{x}_2, \dots, \mathbf{x}_N) = \prod_{i=1}^N \phi_i(\mathbf{x}_i) \quad (2.5)$$

Slater determinant

The expression in 2.5 is a solution for Schrodinger's equation with the Hamiltonian in 2.4. But, it doesn't satisfy the anti-symmetry requirement which states that when we exchange two indistinguishable fermions' coordinates, the wavefunction must exchange its signal. A simple way to satisfy this statement is writing the wavefunction using a Slater determinant. The Slater determinant is made up of single-particle wavefunctions $\phi_i(\mathbf{x}_j)$:

$$\Psi(\mathbf{x}_1, \mathbf{x}_2, \dots, \mathbf{x}_N) = \frac{1}{\sqrt{N!}} \begin{vmatrix} \phi_1(\mathbf{x}_1) & \phi_1(\mathbf{x}_2) & \dots & \phi_1(\mathbf{x}_N) \\ \phi_2(\mathbf{x}_1) & \phi_2(\mathbf{x}_2) & \dots & \phi_2(\mathbf{x}_N) \\ \vdots & \vdots & \dots & \vdots \\ \phi_N(\mathbf{x}_1) & \phi_N(\mathbf{x}_2) & \dots & \phi_N(\mathbf{x}_N) \end{vmatrix} \quad (2.6)$$

We'll use $\mathbf{r}_j \equiv \mathbf{x}_j$ from here, without loss of generality.

Mean-field approximation

Until now, we consider that the electrons are not feeling each other in the system. However, they interact with each other. Classically, a charge density, $n(\mathbf{r})$, generates an electrical potential, $\varphi(\mathbf{r})$, that satisfies Poisson's equation

$$\nabla^2 \varphi(\mathbf{r}) = -4\pi n(\mathbf{r}) \quad (2.7)$$

and another external charge, q , will have $V = q\varphi$ as the potential energy. In our case, as we are working with electrons and $q = -1$, we have $V_H(\mathbf{r}) = -\varphi(\mathbf{r})$ that satisfies also Poisson's equation. Thus, we have

$$\nabla^2 V_H(\mathbf{r}) = 4\pi n(\mathbf{r}) \quad (2.8)$$

and a solution for this differential equation is

$$V_H(\mathbf{r}) = \int d\mathbf{r}' \frac{n(\mathbf{r}')}{|\mathbf{r} - \mathbf{r}'|} \quad (2.9)$$

Here the electron density is given as $n(\mathbf{r}) = \sum_{i=1}^N |\phi_i(\mathbf{r})|^2$, the many-body wavefunction is written as in equation 2.5, and the Hamiltonian is $\hat{H} = \hat{T}_e + \hat{V}_{\text{ext}} + \hat{V}_H$, with V_H the Hartree potential.

Thus, in this approximation, each electron feels a mean-field generated by the other electrons and satisfies the Schrödinger's equation of independent electrons

$$\hat{H}_e \phi_i(\mathbf{r}) = [\hat{T}_e + \hat{V}_{\text{ext}} + \hat{V}_H] \phi_i(\mathbf{r}) = \varepsilon_i \phi_i(\mathbf{r}) \quad (2.10)$$

Hartree-Fock equations

In the mean-field approximation we introduced the electron-electron interaction considering the electrons as classical particles, but we can include this interaction considering the electrons as quantum particles and require that the many-body wavefunction is a Slater determinant of some single-particle wavefunctions. We then use the variational principle, requiring that these single-particle wavefunctions are those that minimize the energy and are orthonormal [20][17]:

$$\frac{\delta E}{\delta \phi_i} = 0, \int \phi_i^*(\mathbf{r})\phi_j(\mathbf{r})d\mathbf{r} = \delta_{ij} \quad (2.11)$$

The expectation value of the energy is

$$E = \int d\mathbf{r}_1 \dots d\mathbf{r}_N \Psi^*(\mathbf{r}_1, \dots, \mathbf{r}_N) \hat{H}_e \Psi(\mathbf{r}_1, \dots, \mathbf{r}_N) \quad (2.12)$$

Using the requirements in equation 2.11, we get the Hartree-Fock equations for the single-particle wavefunctions written as

$$\hat{H}_e \phi_i(\mathbf{r}) = [\hat{T}_e + \hat{V}_{\text{ext}} + \hat{V}_H + \hat{V}_x] \phi_i(\mathbf{r}) = \varepsilon_i \phi_i(\mathbf{r}) \quad (2.13)$$

where \hat{V}_H is the Hartree contribution, 2.9, and \hat{V}_x is the so-called exchange energy. The exchange term arises from the anti-symmetry nature of the single Slater determinant and is a non-local term:

$$\hat{V}_{xj}(\mathbf{r})\phi_i(\mathbf{r}) = \sum_j \left\{ - \int \frac{d\mathbf{r}'}{|\mathbf{r} - \mathbf{r}'|} \phi_j^*(\mathbf{r}')\phi_i(\mathbf{r}') \right\} \phi_j(\mathbf{r}) \quad (2.14)$$

2.2 Density functional theory

Density functional theory (DFT) is a very successful theory in solving the Schrödinger equation for different kinds of quantum systems such as atoms, molecules, and solids, giving a quantitative understanding of their properties [15][16].

As mentioned in subsection 2.1.1, DFT is not the unique method to solve the many-body problem, at least the electronic problem. However, DFT has many advantages over Hartree-Fock (HF) because HF computational effort very quickly grows with increasing N , and description of large systems becomes prohibitive [17][16].

The basic idea of DFT is that any property, in any stationary system of N -interacting fermion particles can be viewed as a functional of the ground state density $n(\mathbf{r})$ [19]. In this sense the total energy, E , is a functional of the density, $E[n]$ [17]. The foundations of this theory are the Hohenberg-Kohn theorems:

- **Theorem I:** For any system of interacting particles in an external potential, $V_{\text{ext}}(\mathbf{r})$, this potential is uniquely determined, except for a constant, by the density of the ground state, $n(\mathbf{r})$.

To demonstrate this theorem, firstly is necessary to solve the Schrödinger equation that, for a non-degenerate system, each $\hat{V}_{\text{ext}}^{(i)}$ gives only one $\Psi^{(i)*}(\mathbf{r}_1, \mathbf{r}_2, \dots, \mathbf{r}_N)$. After that, using the definition of the one-particle density

$$n^i(\mathbf{r}) = N \int \Psi^{(i)*}(\mathbf{r}, \mathbf{r}_2, \dots, \mathbf{r}_N) \Psi^{(i)}(\mathbf{r}, \mathbf{r}_2, \dots, \mathbf{r}_N) d\mathbf{r}_2 \dots d\mathbf{r}_N$$

we obtain that there exists only one $n^i(\mathbf{r})$ for each $\Psi^{(i)*}(\mathbf{r}_1, \mathbf{r}_2, \dots, \mathbf{r}_N)$.

Thus, we assume, by a *reductio ad absurdum*, that two different external potentials $V_{\text{ext}}^i(\mathbf{r})$ and $V_{\text{ext}}^j(\mathbf{r})$, satisfying $V_{\text{ext}}^i(\mathbf{r}) - V_{\text{ext}}^j(\mathbf{r}) \neq \text{const}$, generate the same ground state Ψ^k , i.e.,

$$\hat{H}^{(i)}\Psi^k = [\hat{T}_e + \hat{V}_{\text{int}} + \hat{V}_{\text{ext}}^{(i)}]\Psi^k = E^{(i)}\Psi^k \quad \text{and} \quad \hat{H}^{(j)}\Psi^k = [\hat{T}_e + \hat{V}_{\text{int}} + \hat{V}_{\text{ext}}^{(j)}]\Psi^k = E^{(j)}\Psi^k$$

Subtraction of these two expressions gives

$$[\hat{V}_{\text{ext}}^{(i)} - \hat{V}_{\text{ext}}^{(j)}]\Psi^k = (E^{(i)} - E^{(j)})\Psi^k$$

This result is false because, by construction, $V_{\text{ext}}^i(\mathbf{r}) - V_{\text{ext}}^j(\mathbf{r}) \neq \text{const}$.

To conclude the second part we assume that two different ground states Ψ^i and Ψ^j , of different systems, generate the same ground state density $n^i(\mathbf{r}) = n^j(\mathbf{r})$. Thus,

$$\langle \Psi^{(i)} | \hat{H}^{(i)} | \Psi^{(i)} \rangle = E^{(i)} \quad (2.15)$$

and

$$\langle \Psi^{(j)} | \hat{H}^{(j)} | \Psi^{(j)} \rangle = E^{(j)} \quad (2.16)$$

The variational principle ensures that $\langle \Psi^{(i)} | \hat{H}^{(j)} | \Psi^{(i)} \rangle > E^{(j)}$ and $\langle \Psi^{(j)} | \hat{H}^{(i)} | \Psi^{(j)} \rangle > E^{(i)}$.

The only difference between the Hamiltonians is the external potentials and, using their definitions, we get

$$\begin{aligned} \langle \Psi^{(i)} | \hat{T}_e + \hat{V}_{\text{int}} + \hat{V}_{\text{ext}}^{(j)} | \Psi^{(i)} \rangle > E^{(j)} &\iff \langle \Psi^{(i)} | \hat{H}^{(i)} | \Psi^{(i)} \rangle + \langle \Psi^{(i)} | \hat{V}_{\text{ext}}^{(j)} - \hat{V}_{\text{ext}}^{(i)} | \Psi^{(i)} \rangle > E^{(j)} \iff \\ &\iff E^{(i)} + \langle \Psi^{(i)} | \hat{V}_{\text{ext}}^{(j)} - \hat{V}_{\text{ext}}^{(i)} | \Psi^{(i)} \rangle > E^{(j)} \end{aligned} \quad (2.17)$$

We can use the same steps to show that with $\langle \Psi^{(j)} | \hat{H}^{(i)} | \Psi^{(j)} \rangle > E^{(i)}$, we have

$$\langle \Psi^{(j)} | \hat{V}_{\text{ext}}^{(i)} - \hat{V}_{\text{ext}}^{(j)} | \Psi^{(j)} \rangle + E^{(j)} > E^{(i)} \quad (2.18)$$

For $\hat{H}^{(i)}$ and $\Psi^{(i)}$, we have that $\langle \Psi^{(i)} | \hat{H}^{(i)} | \Psi^{(i)} \rangle = \langle \Psi^{(i)} | \hat{T}_e | \Psi^{(i)} \rangle + \langle \Psi^{(i)} | \hat{V}_{\text{int}} | \Psi^{(i)} \rangle + \int d\mathbf{r} \hat{V}_{\text{ext}}^{(i)} n^i(\mathbf{r})$, thus, if $\Psi^{(i)}$ and $\Psi^{(j)}$ both generate the density $n^i(\mathbf{r}) = n^j(\mathbf{r})$, that means that, by definition of the one-particle density, $\Psi^{(i)}$ is equal to $\Psi^{(j)}$. The density is equal. Then, because the external potentials are multiplicative (are local), the sum of the last two inequalities 2.17 and 2.18 gives

$$E^{(i)} + E^{(j)} > E^{(j)} + E^{(i)} \quad (2.19)$$

This inequality, 2.19, is obviously an absurd, and shows that for each ground state, $\Psi^{(i)}$, there is only one ground state density, $n^i(\mathbf{r})$ and vice-versa. Thus, $\hat{V}_{\text{ext}}^{(i)}$, $\Psi^{(i)}$ and $n^i(\mathbf{r})$ determine each other uniquely [21], and we have fully demonstrated the first Hohenberg-Kohn theorem.

With the first theorem demonstrated, we conclude that the wavefunction is a functional of the density, $\Psi[n(\mathbf{r})]$, by mapping n to Ψ .

The second theorem is implicit in the first one when we consider that only $V_{\text{ext}}(\mathbf{r})$ can change the Hamiltonian for a given number of electron. Indeed, this means that we take the $\hat{T}_e + \hat{V}_{\text{int}}$ as a universal term for all N-electron systems defining a universal functional $F[n]$. Thus, the ground state energy can be written as

$$E_{\text{Vi}}^i[n^i] = F[n^i] + \int d\mathbf{r} V^i(\mathbf{r}) n^i(\mathbf{r})$$

The second theorem states that:

- **Theorem II:** For any particular external potential $V_{\text{ext}}(\mathbf{r})$, the global minimum value of the energy functional of a system is the exact ground state energy, and the density $n(\mathbf{r})$ that minimizes the energy functional is the exact ground state density.

Again, the variational principle ensures that if $V_{\text{ext}}(\mathbf{r})$ has the corresponding ground state $n(\mathbf{r})$, then for other density $n'(\mathbf{r})$ we have

$$E[n'(\mathbf{r})] = \langle \Psi' | \hat{H} | \Psi' \rangle = F[n'(\mathbf{r})] + \int d\mathbf{r} V_{\text{ext}}(\mathbf{r}) n'(\mathbf{r}) > \langle \Psi | \hat{H} | \Psi \rangle = E[n(\mathbf{r})]$$

2.2.1 The Kohn-Sham approach

A good way to introduce the Kohn-Sham approach is consider a system of non-interacting electrons in a multiplicative potential v_s . The Hamiltonian of this system is $\hat{H} = \hat{T} + \hat{V}_s$ with $\hat{V}_s = \int d\mathbf{r} n(\mathbf{r}) v_s(\mathbf{r})$ and its N-particle ground state a Slater determinant Ψ_0 with the non-interacting Kohn-Sham density n_0 . This Slater determinant is constructed from the energetically lowest solutions ϕ_i of the single-particle Schrödinger equation $\left\{ -\frac{\nabla^2}{2} + v_s \right\} \phi_i = \varepsilon_i \phi_i$. The Kohn-Sham assumption is that there exists a non-interacting system whose density is the density of the interacting system under study. This parallelism implies that the structure of v_s reflects the nature of the interacting system[21].

Thus, the Kohn-Sham idea is the exchanging the many-body interacting problem by a single-particle system, splitting the universal functional, $F[n]$, in terms such as that in the Mean-field Approximation, 2.10, plus an extra term which includes the many-body effects, exchange and correlation effects, $E_{\text{xc}}[n]$. That is, the total energy is

$$E[n] = \int d\mathbf{r} V_{\text{ext}}(\mathbf{r}) n(\mathbf{r}) - \sum_i \int d\mathbf{r} \phi_i^*(\mathbf{r}) \frac{\nabla^2}{2} \phi_i(\mathbf{r}) + \frac{1}{2} \int d\mathbf{r} \int d\mathbf{r}' \frac{n(\mathbf{r}) n(\mathbf{r}')}{|\mathbf{r} - \mathbf{r}'|} + E_{\text{xc}}[n] \quad (2.20)$$

This equation tells us that we know all the three initial terms, and if we knew the last one, then we could calculate, using the density, the system's total energy in its ground state[17].

To determine the density, we use the variational principle, stating that

$$\frac{\delta E[n]}{\delta \phi_i^*(\mathbf{r})} = 0$$

with $\phi_i(\mathbf{r})$ orthonormal between them, and we get the Kohn-Sham equations rewritten as

$$\left[-\frac{\nabla^2}{2} + V_{\text{ext}} + V_{\text{H}} + V_{\text{xc}} \right] \phi_i(\mathbf{r}) = \varepsilon_i \phi_i(\mathbf{r}) \quad (2.21)$$

with $V_{\text{xc}} = \frac{\delta E_{\text{xc}}[n]}{\delta n(\mathbf{r})}$, the so-called exchange-correlation potential. The density here is determined by expression $n(\mathbf{r}) = \sum_i |\phi_i(\mathbf{r})|^2$. And we have a self-consistency problem.

Thus, if we know the exact form of E_{xc} , we can determine exactly the properties of the system.

To be more clear, the wavefunctions $\phi_i(\mathbf{r})$ are fictitious, and the only requirement is that the density of our fictitious non-interacting system where these $\phi_i(\mathbf{r})$ are the true solutions is equal to the real electron density. Now all our attention is concerned with the term we don't know, and constructing useful approximations for that.

2.2.2 Local density approximation

There are several degrees of approximation for the exchange-correlation functional. These degrees obey the Jacob's Ladder [14]. For the goal of this job, we will be concerned only with the more simple class. This class however, is reasonably accurate in practical calculations. This class is the so-called Local Density Approximation, LDA.

In the Kohn-Sham approach, the unknown term, $E_{\text{xc}}[n]$, can reasonably be approximated as a local or nearly local functional of the density, i.e, we can write $E_{\text{xc}}[n]$ as

$$E_{\text{xc}}[n] = \int d\mathbf{r} n(\mathbf{r}) \epsilon_{\text{xc}}([n], \mathbf{r}) \quad (2.22)$$

with $\epsilon_{\text{xc}}[n]$ exchange-correlation energy per electron at position \mathbf{r} , depending only upon the density $n(\mathbf{r})$ in some neighborhood of point \mathbf{r} [19].

Kohn and Sham, in 1965, proposed a way to write the exchange-correlation functional by considering a sort of locally homogeneous gas. In this approximation, a small volume in space contributes the same exchange-correlation energy as an equal volume of a homogeneous electron gas at the same density [22][15]. In this case the exchange-correlation energy is given as $E_{\text{xc}}[n] = \int d\mathbf{r} n(\mathbf{r}) \epsilon_{\text{xc}}[n]$ and $V_{\text{xc}} = (\epsilon_{\text{xc}}[n] + n \frac{d\epsilon_{\text{xc}}[n]}{dn})$.

It is expected that this approximation works well in systems where the true density is close to a homogeneous gas (like a nearly free-electron metal) and it is not expected to work for very inhomogeneous systems such as atoms [19].

In the Hartree-Fock theory of free electrons, the contribution of the exchange term to the total energy is given by, in atomic units,

$$E_x = -\frac{3}{4} \frac{1}{\pi} k_F N = -\frac{3}{4} \frac{1}{\pi} \int k_F n d\mathbf{r} = -\frac{3}{4} \left(\frac{3}{\pi}\right)^{\frac{1}{3}} \int n^{\frac{1}{3}} n d\mathbf{r}$$

where $N = \int n d\mathbf{r}$ and $k_F = (3\pi^2 n)^{1/3}$. Using this as a start point, we can generalize to situations with non-uniform density and assume the general expression as

$$E_x[n] = \int d\mathbf{r} n(\mathbf{r}) \epsilon_x[n] \quad (2.23)$$

with $\epsilon_x([n]) = -\frac{3}{4} \left(\frac{3}{\pi}\right)^{\frac{1}{3}} n^{\frac{1}{3}}$. The exchange potential is, in this case, $V_x = -\left(\frac{3}{\pi}\right)^{\frac{1}{3}} n^{\frac{1}{3}}$. But we know that there are other many-body effects that we shall designate by the

correlation. The LDA is based upon this exchange energy and a lot of approximations and fitting to numerical correlation energies for the homogeneous gas[19].

We don't know the exact form of the correlation term, but there are asymptotic forms for the homogeneous electrons gas in the high and low density limits [23]:

- for the high-density limit ($r_s \rightarrow 0$)

$$\epsilon_c[n] = c_0 \ln r_s - c_1 + c_2 r_s \ln r_s - c_3 r_s + \dots \quad (2.24)$$

with $c_0 = 0.031091$ and $c_1 = 0.046644$

- for low-density limit ($r_s \rightarrow \infty$)

$$\epsilon_c[n] = \frac{1}{2} \left(-\frac{d_0}{r_s} + \frac{d_1}{r_s^{3/2}} + \dots \right) \quad (2.25)$$

where $r_s = \left(\frac{3}{4\pi n}\right)^{1/3}$. The correlation term, in the Perdew-Zunger parametrization, has the formulae [19]:

- for $r_s < 1$:

$$\epsilon_c^{PZ}[n] = -0.0480 + 0.031 \ln r_s - 0.0116 r_s + 0.0020 r_s \ln r_s \quad (2.26)$$

- for $r_s > 1$:

$$\epsilon_c^{PZ}[n] = -0.1423 / (1 + 1.0529\sqrt{r_s} + 0.3334r_s) \quad (2.27)$$

and then, given ϵ_x and ϵ_c , we can construct $\epsilon_{xc} = \epsilon_x + \epsilon_c$ and introduce this into

$$E_{xc}[n] = \int d\mathbf{r} n(\mathbf{r}) \epsilon_{xc}[n] \quad (2.28)$$

2.3 Self-consistency

We have seen that in the single-particle picture, the electronic density is given by

$$n(\mathbf{r}) = \sum_i |\phi_i(\mathbf{r})|^2 \quad (2.29)$$

and, from equations 2.21, 2.13 we see that the effective potential depends on the solution of the Schrodinger equation. This means that each orbital $\phi_i(\mathbf{r})$ can be determined by solving the corresponding single-particle Schrodinger's equation, if all other orbitals $\phi_j(\mathbf{r})$, $j \neq i$ [2] were known. In other words, our Hamiltonian depends on its eigenstates[20]. That is a self-consistency problem, and solving the equations must be done iteratively. In practice, we start with a guess, a set of trial wavefunctions with which we construct the effective potential. After that, solving Schrödinger's equation, we compare the resulting new wavefunctions with the older ones. This procedure continues until new and old wavefunctions are the same. Schematically it's illustrated in Figure 2.1.

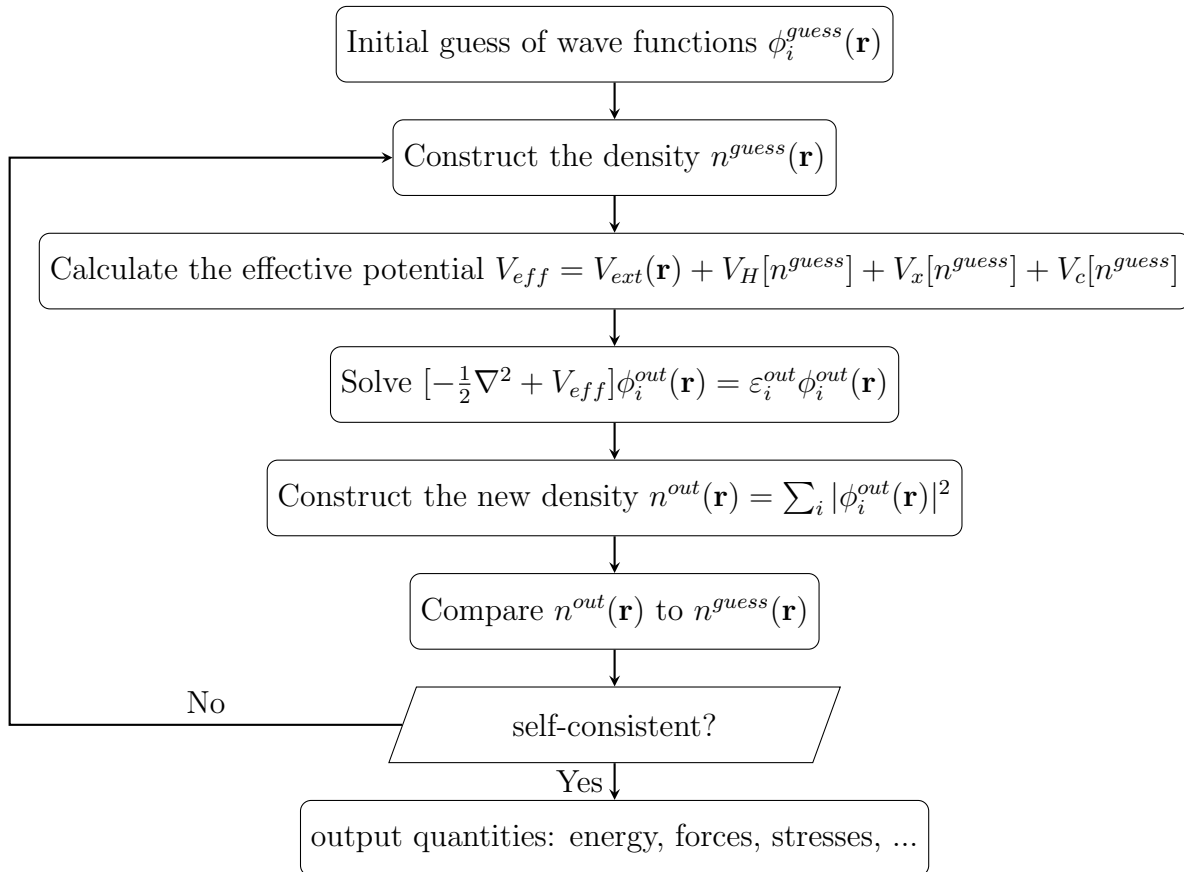


Figure 2.1: Schematic representation of the self-consistent loop.

2.4 Density functional perturbation theory

As we mentioned earlier, the electronic and ionic subsystems both define the matter's properties. A wide variety of physical properties of solids depend on their lattice-dynamical behavior. The heat capacity is an example of such properties. The resistivity of metals and superconductivity are physical phenomena related to the electron-phonon² interaction.

2.4.1 The lattice vibrations and electronic structure theory

After solving the electronic problem, we introduce the ionic problem, vibrations of the lattice, as a perturbation. We consider that the ions are moving in a potential energy surface provided by the solution of the electronic problem[20][22]. Thus for dynamical properties, we must solve the Schrodinger equation given as

$$\left\{ -\sum_I \frac{1}{2M_I} \nabla_I^2 + E(\mathbf{R}) \right\} \Phi(\mathbf{R}) = \xi \Phi(\mathbf{R}) \quad (2.30)$$

²In section 3.2 we talk about phonons

where $E(\mathbf{R})$ is the ground state eigenvalue in 2.3 plus the ion-ion interaction contribution, $\hat{E}_{nn} = \sum_{I < J} \frac{Z_I Z_J}{|\mathbf{R}_I - \mathbf{R}_J|}$ ³, \mathbf{R}_I is the coordinate of the I^{th} nucleus, M_I its mass, and $\mathbf{R} \equiv \{\mathbf{R}_I\}$.

By definition, the force acting on the I^{th} nucleus is given as the negative of the gradient of the potential $E(\mathbf{R})$ with respect to the position \mathbf{R}_I and the equilibrium condition requires that the forces acting on the individual nuclei must be equal to zero. That is

$$\mathbf{F}_I = -\frac{\partial E(\mathbf{R})}{\partial \mathbf{R}_I} = 0 \quad (2.31)$$

On the other hand, vibrational frequencies of a nucleus, ω , are eigenvalues of the Hessian of the potential energy surface scaled by the nuclear masses

$$\det \left(\frac{1}{\sqrt{M_I M_J}} \frac{\partial^2 E(\mathbf{R})}{\partial \mathbf{R}_I \partial \mathbf{R}_J} - \omega^2 \right) = 0 \quad (2.32)$$

2.4.2 Hellmann-Feynman theorem

The equilibrium condition and evaluation of nuclei's vibrational frequencies require calculations of derivatives of the potential, the electronic ground state eigenvalue, $E(\mathbf{R})$. To do this, we use the Hellmann-Feynman theorem. This theorem states that with the eigenvalue problem

$$\hat{H}\Psi_\lambda = E_\lambda \Psi_\lambda$$

where λ is a parameter, nuclei positions, for example, the derivative of the eigenvalue is given by

$$\frac{\partial E_\lambda}{\partial \lambda} = \langle \Psi_\lambda | \frac{\partial \hat{H}_\lambda}{\partial \lambda} | \Psi_\lambda \rangle \quad (2.33)$$

For our case, this means that we can evaluate the forces as

$$\mathbf{F}_I = -\langle \Psi_{\mathbf{R}} | \frac{\partial}{\partial \mathbf{R}_I} \left\{ -\sum_i \frac{1}{2} \nabla_i^2 + \sum_{i < j} \frac{1}{|\mathbf{r}_i - \mathbf{r}_j|} + \sum_{I < J} \frac{Z_I Z_J}{|\mathbf{R}_I - \mathbf{R}_J|} - \sum_{i, I} \frac{Z_I}{|\mathbf{R}_I - \mathbf{r}_i|} \right\} | \Psi_{\mathbf{R}} \rangle \quad (2.34)$$

where the first and second terms on the derivative are zero, and we get

$$\mathbf{F}_I = -\langle \Psi_{\mathbf{R}} | \frac{\partial V_{\mathbf{R}}(\mathbf{r})}{\partial \mathbf{R}_I} + \frac{\partial E_{nn}(\mathbf{R})}{\partial \mathbf{R}_I} | \Psi_{\mathbf{R}} \rangle = -\int n_{\mathbf{R}}(\mathbf{r}) \frac{\partial V_{\mathbf{R}}(\mathbf{r})}{\partial \mathbf{R}_I} d\mathbf{r} - \frac{\partial E_{nn}(\mathbf{R})}{\partial \mathbf{R}_I} \quad (2.35)$$

Here $V_{\mathbf{R}}(\mathbf{r}) \equiv V_{ext}(\mathbf{r}) = \sum_{i, I} \frac{Z_I}{|\mathbf{R}_I - \mathbf{r}_i|}$. Using equation 2.38 we determine the Hessian in equation 2.35 as

$$\frac{\partial^2 E(\mathbf{R})}{\partial \mathbf{R}_I \partial \mathbf{R}_J} = -\frac{\partial \mathbf{F}_I}{\partial \mathbf{R}_J} = \int \left\{ \frac{\partial n_{\mathbf{R}}(\mathbf{r})}{\partial \mathbf{R}_J} \frac{\partial V_{\mathbf{R}}(\mathbf{r})}{\partial \mathbf{R}_I} + n_{\mathbf{R}}(\mathbf{r}) \frac{\partial^2 V_{\mathbf{R}}(\mathbf{r})}{\partial \mathbf{R}_I \partial \mathbf{R}_J} \right\} d\mathbf{r} + \frac{\partial^2 E_{nn}(\mathbf{R})}{\partial \mathbf{R}_I \partial \mathbf{R}_J} \quad (2.36)$$

The first derivative of the ground state electronic density with respect to the nucleus, $\partial n_{\mathbf{R}}(\mathbf{r}) / \partial \mathbf{R}_J$, is called *linear response* to a distortion of the nuclear geometry. The Hessian here represents the interatomic force constants. Thus, the equation 2.39 tells us that to calculate the nuclei frequencies of oscillation is necessary to know the ground

³We neglected this term in the electronic problem because, for fixed nuclear positions, it is a constant, and a constant has no effect on the operator eigenfunctions[20]

state electronic density and its change as a consequence of a distortion of the nuclear geometry, linear response. Here lives the main object of density functional perturbation theory; evaluation of the linear response after all calculations using density functional theory.

2.4.3 Linear response

To determine the linear response, we can use our definition of electronic density in the single-particle picture, equation 2.29, and linearize it as

$$n_{\mathbf{R}}(\mathbf{r}) = \sum_i \phi_i^*(\mathbf{r}; \mathbf{R}) \phi_i(\mathbf{r}; \mathbf{R})$$

$$\sum_I \frac{\partial n_{\mathbf{R}}(\mathbf{r})}{\partial \mathbf{R}_I} d\mathbf{R}_I \equiv \Delta n(\mathbf{r}) = 2Re \sum_i \phi_i^*(\mathbf{r}; \mathbf{R}) \sum_I \frac{\partial \phi_i(\mathbf{r}; \mathbf{R})}{\partial \mathbf{R}_I} d\mathbf{R}_I =$$

$$2Re \sum_i \phi_i^*(\mathbf{r}; \mathbf{R}) \Delta \phi_i(\mathbf{r}; \mathbf{R}) \quad (2.37)$$

The external potential is real, which means that the Kohn-Sham wavefunctions and their complex conjugate are degenerate, and the imaginary part in equation 2.37 is zero.

To determine the variation of the wavefunction, $\Delta \phi_i$, we use first-order perturbation theory.

$$(H_{SCF} - \varepsilon_i) \Delta \phi_i = (\Delta \varepsilon_i - \Delta V_{SCF}) \phi_i \quad (2.38)$$

with its solution given as

$$\Delta \phi_i(\mathbf{r}) = \sum_{j \neq i} \phi_j(\mathbf{r}) \frac{\langle \phi_j | \Delta V_{SCF} | \phi_i \rangle}{\varepsilon_i - \varepsilon_j} \quad (2.39)$$

where H_{SCF} is the full Kohn-Sham Hamiltonian, equation 2.21, and V_{SCF} is its associated effective potential. Thus the first-order variation of the Kohn-Sham eigenvalues ε_i is given as

$$\Delta \varepsilon_i = \langle \phi_i | \Delta V_{SCF} | \phi_i \rangle \quad (2.40)$$

and the first-order correction to the effective potential, ΔV_{SCF} , is

$$\Delta V_{SCF}(\mathbf{r}) = \Delta V_{ext}(\mathbf{r}) + \int \frac{\Delta n(\mathbf{r}')}{|\mathbf{r} - \mathbf{r}'|} d\mathbf{r}' + \frac{dV_{xc}(n)}{dn} \Delta n(\mathbf{r}) \quad (2.41)$$

Now we can substitute equation 2.39 in equation 2.37, and we get the linear response given as

$$\Delta n(\mathbf{r}) = 2 \sum_i \sum_{j \neq i} \phi_i^*(\mathbf{r}) \phi_j(\mathbf{r}) \frac{\langle \phi_j | \Delta V_{SCF} | \phi_i \rangle}{\varepsilon_i - \varepsilon_j} \quad (2.42)$$

Equations 2.38, 2.41, 2.42 form a set of self-consistent equations for the perturbed system and this self-consistency requirement manifests itself in the dependence of the right-hand side upon the solution of the linear system, 2.38 [22]. This procedure is important because it will help us to calculate phonon frequencies, as is described in the next chapter.

2.5 Pseudopotential Approximation

Not all electrons contribute equally to the physical properties of materials. We can consider that only the valence electrons contribute, that is, core electrons remain essentially inactive [24] such that many electronic structure properties such as bonding, ground and excited states, and their related properties depend almost only on the valence electrons [25]. Then, we have a natural separation between electrons in core and valence electrons, which is the principal idea behind the pseudopotential approximation.

The decomposition of states into active and inert states is done for most atoms. For example, in a silicon atom the $1s^2 2s^2 2p^6$ core states are tightly bound compared to the $3s^2 3p^2$ valence states [1]. The following image shows the concept of ionic cores for a crystalline solid, with each atomic nucleus and its core electrons forming the ion core.

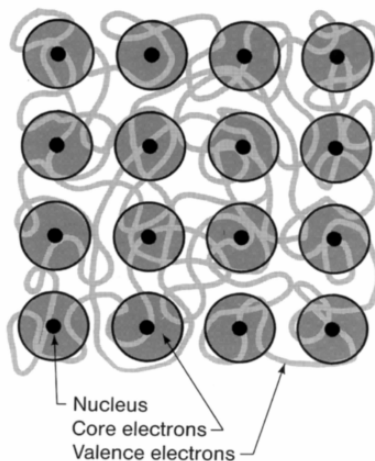


Figure 2.2: Model of a solid and valence electrons using ionic cores [1].

Actually, with this approximation, we are replacing the Coulomb potential in the many-electron system Hamiltonian with an effective potential so that the electron wavefunctions oscillating rapidly in the core region are replaced by nodeless pseudo-wavefunctions having the right energy and the same outer range properties [26].

To develop the pseudopotential for a specific atom, we consider it as isolated and denote the solutions of single-particle equations, for the atom, by $|\psi^{(n)}\rangle$ [2]. Thus, separating the core electron, $|\psi^c\rangle$, from the valence electrons, $|\psi^v\rangle$, both wavefunctions must satisfy the single-particle equations

$$\hat{H}|\psi^v\rangle = \varepsilon^v|\psi^v\rangle \quad (2.43)$$

$$\hat{H}|\psi^c\rangle = \varepsilon^c|\psi^c\rangle \quad (2.44)$$

We can define a new set of smooth valence states $|\phi^v\rangle$ such that

$$|\psi^v\rangle = |\phi^v\rangle + \sum_c a_c |\psi^c\rangle \quad (2.45)$$

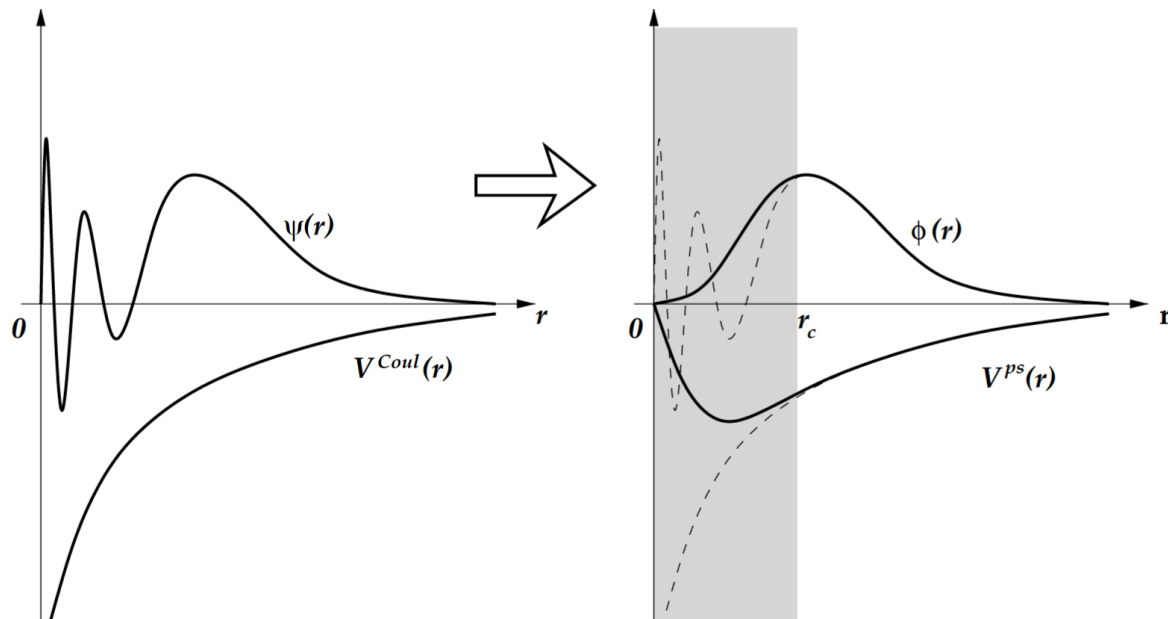


Figure 2.3: Schematic representation of the construction of the pseudo-wavefunction ϕ and pseudopotential V^{ps} [2].

with $|\phi^v\rangle$ non-orthogonal to $|\psi^c\rangle$, but $|\psi^c\rangle$ and $|\psi^v\rangle$ are orthogonal between them. In this way, we can make inner product with $\langle\psi^c|$ and get the result

$$\begin{aligned} \langle\psi^c|\psi^v\rangle &= \langle\psi^c|\phi^v\rangle + \sum_c^I a'_c \langle\psi^c|\psi^c\rangle \iff \langle\psi^c|\phi^v\rangle + a_c = 0 \Rightarrow \\ &\Rightarrow |\psi^v\rangle = |\phi^v\rangle - \sum_c \langle\psi^c|\phi^v\rangle |\psi^c\rangle \quad (2.46) \end{aligned}$$

Replacing equation 2.46 in equation 2.43, and using the equation 2.44 we get

$$\begin{aligned} \hat{H}|\phi^v\rangle - \sum_c \langle\psi^c|\phi^v\rangle \hat{H}|\psi^c\rangle &= \varepsilon^v \{ |\phi^v\rangle - \sum_c \langle\psi^c|\phi^v\rangle |\psi^c\rangle \} \iff \\ \iff \{ \hat{H} - \sum_c \varepsilon^c |\psi^c\rangle \langle\psi^c| \} |\phi^v\rangle &= \varepsilon^v \{ 1 - \sum_c |\psi^c\rangle \langle\psi^c| \} |\phi^v\rangle \Rightarrow \\ \Rightarrow \{ \hat{H} + \sum_c (\varepsilon^v - \varepsilon^c) |\psi^c\rangle \langle\psi^c| \} |\phi^v\rangle &= \varepsilon^v |\phi^v\rangle \quad (2.47) \end{aligned}$$

That means that the new set of valence electron states, $|\phi^v\rangle$, obeys a single-particle equation with a new potential, but with the same eigenvalues, ε^v , as the original valence electron states $|\psi^v\rangle$. The new set of valence states we call pseudo-wavefunctions and we have a new potential which we call pseudopotential, $\hat{V} + \sum_c (\varepsilon^v - \varepsilon^c) |\psi^c\rangle \langle\psi^c|$.

The pseudopotential incorporating the core electrons is smoother than the original nucleus potential at the origin. It is because the repulsive contribution from the core electrons cancels a part of the Coulomb's attractive potential from the nucleus. However, farther away from the core domain where the core states decay exponentially, the valence states feel the original Coulomb potential, as it's possible to see in figure 2.3.

Although the potential is weak and only binds the valence state, this potential is energy-dependent, state-dependent, and involves a non-local, non-Hermitian operator, $(\sum_c(\varepsilon^v - \varepsilon^c)|\psi^c\rangle\langle\psi^c|)|\phi^v\rangle = \int V^{ps}(\mathbf{r}, \mathbf{r}')\phi^v(\mathbf{r}')d\mathbf{r}'$ with $V^{ps}(\mathbf{r}, \mathbf{r}') = \sum_c(\varepsilon^v - \varepsilon^c)\psi^{c*}(\mathbf{r}')\psi^c(\mathbf{r})$, and the pseudopotential is not unique. These problems make the pseudopotential within this construction more complex than the original potential. However, the practice of this art has shown that these features can actually be exploited to define pseudopotentials that work very well in reproducing the behavior of the valence wavefunctions in the regions outside the core, which are precisely the regions of interest for the physics of solids [1][2][19].

2.5.1 Norm conserving pseudopotential

As we mentioned above, the pseudowavefunctions $|\phi^v\rangle$ are not orthonormal because the complete function $|\psi^v\rangle$ also contains the sum over core orbitals, equation 2.46[19].

One of the most widely used type of pseudopotentials is the family of norm-conserving pseudopotentials.

Essentially, five properties must be satisfied in the norm-conserving construction of pseudopotentials[27][28][19]:

- All-electron and pseudovalence eigenvalues agree for the chosen atomic reference configuration;
- All-electron and pseudovalence wavefunctions agree beyond a chosen core radius r_c ;
- The logarithmic derivatives of all-electron and pseudowavefunctions agree at r_c ;
- The integrated charge inside r_c for each wavefunction agrees (norm conservation);
- The first energy derivative of the logarithmic derivatives of the all-electron and pseudowavefunctions agrees at r_c , and therefore for all $r \geq r_c$

The first and second items guarantee that the atomic pseudopotential outside the core-region is equal to the original potential; the third property guarantees that the scattering properties of the pseudopotential match those of the full potential

$$D_l(\varepsilon, r) = r\psi'_l(\varepsilon, r)/\psi_l(\varepsilon, r) = r\frac{d}{dr} \ln \psi_l(\varepsilon, r) \quad (2.48)$$

with ψ representing the all-electron wavefunction and also the pseudowavefunction with angular momentum l , and the prime represents derivation of the function. The norm conservation, inside r_c , means the total charge inside must equal for both wavefunctions

$$Q_l = \int_0^{r_c} dr r^2 |\psi_l(r)|^2 = \int_0^{r_c} dr r^2 |\phi_l(r)|^2 \quad (2.49)$$

This in turn guarantees that scattering at energies close to ε is well described.

In equation 2.49, $\psi_l(r)$ and $\phi_l(r)$ represent all-electron radial orbital and its pseudowavefunction. Property five is crucial toward the goal of constructing a good pseudopotential, i.e, one that is generated in a spherical atom and can be used in a more

complex environment[19]. Indeed, we need to calculate $\frac{\partial D_l(\varepsilon, r)}{\partial \varepsilon}$ and for that, we consider the Kohn-Sham radial equation for a spherical atom which can be written as

$$-\frac{1}{2} \frac{d^2 \phi_l(r)}{dr^2} + \left\{ \frac{l(l+1)}{2r^2} + V^{eff} - \varepsilon \right\} \phi_l(r) = 0 \quad (2.50)$$

with V^{eff} the atomic's effective potential in the Kohn-Sham procedure. Using the definition

$$x_l(\varepsilon, r) \equiv \frac{\partial}{\partial r} \ln \phi_l(\varepsilon, r) = \frac{1}{\phi_l(\varepsilon, r)} \frac{\partial \phi_l(\varepsilon, r)}{\partial r} \quad (2.51)$$

differentiating this with respect to r , it's possible to show that we get the following equation

$$\frac{\partial x_l}{\partial r} + x_l^2 = \frac{l(l+1)}{2r^2} + 2(V^{eff} - \varepsilon) \quad (2.52)$$

Differentiating the equation 2.52 with respect to the energy, and rewriting $\frac{\partial}{\partial \varepsilon} \frac{\partial x_l}{\partial r}$ as $\frac{\partial}{\partial r} \frac{\partial x_l}{\partial \varepsilon}$ gives

$$\frac{\partial}{\partial r} \frac{\partial x_l}{\partial \varepsilon} + 2x_l \frac{\partial x_l}{\partial \varepsilon} = -2 \quad (2.53)$$

Using the relation valid for any function $f(r)$ and any l

$$f' + 2x_l f = \frac{1}{\phi_l^2} \frac{\partial}{\partial r} (\phi_l^2 f) \quad (2.54)$$

and comparing with the equation 2.53, we obtain $f(r) = \frac{\partial x_l}{\partial \varepsilon}$. Thus, we can show that at radius r_c , we get

$$\frac{\partial x_l(\varepsilon, r_c)}{\partial \varepsilon} = -\frac{2}{\phi_l^2(r_c)} \int_0^{r_c} dr \phi_l^2 = -\frac{2Q_l(r_c)}{\phi_l^2(r_c)} \quad (2.55)$$

or, in terms of D_l

$$\frac{\partial D_l(\varepsilon, r_c)}{\partial \varepsilon} = -\frac{2r_c}{\phi_l^2(r_c)} \int_0^{r_c} dr \phi_l^2 = -\frac{2r_c}{\phi_l^2(r_c)} Q_l(r_c) \quad (2.56)$$

Thus, we have shown that $\frac{\partial x_l}{\partial \varepsilon}$ and $\frac{\partial D_l}{\partial \varepsilon}$ are the same for the pseudo and all-electron wavefunction if ϕ_l obeys the norm-conservation [19].

Chapter 3

Superconductivity

3.1 Periodic solids and electronic bands

When ions are chemically bound to one another and have well-defined equilibrium separations determined by the condition that the total energy is minimum and leads to a three-dimensional periodic arrangement, we say that they are in a 3D crystalline state. In a crystalline state, we can predict the positions, points of the lattice, of all other atoms if we know the stationary points of a few ions. This set of a few ions forms periodically repeated units [29][30].

A 3D lattice is spanned by three vectors \mathbf{a} , \mathbf{b} and \mathbf{c} , and every point (lattice point) on the lattice can be reached by a translation operation given by

$$\mathbf{T} = n_1\mathbf{a} + n_2\mathbf{b} + n_3\mathbf{c} \quad (3.1)$$

i.e, we can reach \mathbf{r}' from \mathbf{r} using \mathbf{T} as

$$\mathbf{r}' = \mathbf{r} + \mathbf{T} = \mathbf{r} + n_1\mathbf{a} + n_2\mathbf{b} + n_3\mathbf{c} \quad (3.2)$$

where n_1 , n_2 and n_3 are integers, and \mathbf{a} , \mathbf{b} and \mathbf{c} are called the fundamental translation vectors or basis vector or, also, crystal axes. If the transformation in equation 3.2 is possible with non-integral n_1 , n_2 , and n_3 , then the \mathbf{a} , \mathbf{b} , and \mathbf{c} vectors are said to be non-primitive translation vectors[31].

The translation vectors form parallelograms called unit cells, and if n_1 , n_2 , and n_3 are any integers, then the unit cell is also called primitive. Thus, for any values of n_1 , n_2 , and n_3 , the translation operation takes us from a unit cell to another. A unit cell may contain an ion or a collection of them. Any primitive unit cell contains only one lattice point [32][31]. There are many possibilities for a primitive unit cell, but always one can choose a primitive cell with the following construction:

- using one lattice point, connect it to all its nearby lattice points, and for each connector line at the midpoint, draw a normal

The volume enclosed by these normals is a primitive unit cell (Wigner-Seitz cell).

The Wigner-Seitz cell is the most common choice, although a non-primitive unit cell can be selected as the conventional unit cell if this possesses higher symmetry than the primitive unit cell[31].

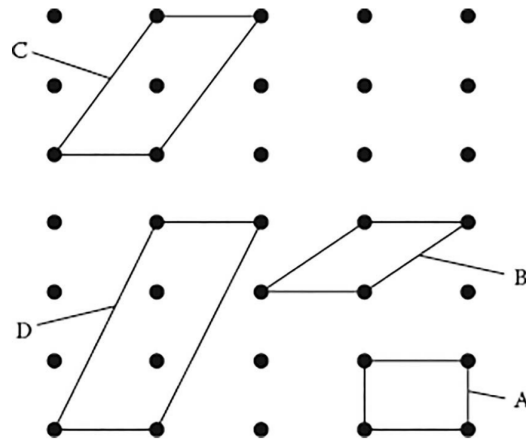


Figure 3.1: Primitive (A and B) and non-primitive (C and D) 2D unit cells [3].

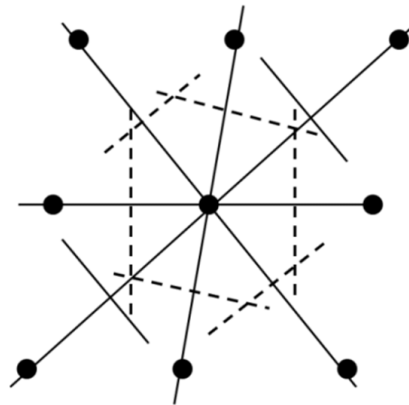


Figure 3.2: Construction of Wigner-Seitz cell (the hexagon inscribed by the dashed lines)[4].

3.1.1 Fundamental types of three-dimensional lattices

The translation symmetry operation is not the only one in crystalline solids. There are other symmetry operations, such as rotation, reflection, and inversion. These symmetry operations also transform crystals into themselves. The rotation operation is a rotation operation about an axis that passes along a lattice point. Lattices can rotate by $2\pi/n$ around an axis, then called n -fold rotation axes with $n = 1, 2, 3, 4, 6$. If there exists a plane in the lattice which divides the lattice into two identical halves and these halves are mirror images of each other, then we can, by reflection operation, exchange them, and the lattice remains the same. It's possible to have mirror reflections m about a plane through a lattice point. The inversion symmetry operation (which is only for three dimensions) implies that each point located at \mathbf{r} relative to a lattice point has an identical point located at $-\mathbf{r}$ relative to the same lattice point [33][31].

The lattice point group is the collection of symmetry operations that, when applied to a lattice point, carries the lattice into itself. The symmetry operations are helpful for the classification of crystal structures (lattice + basis¹) by comparing the symmetry of

¹An ion or group of placed at each lattice point in regular fashion

different point groups. There are 32 different point groups. However, lattices consistent with the point group operations are limited and form the so-called Bravais lattices, which are fourteen, grouped into seven crystal systems as is showing in the Table 3.3.

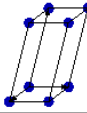
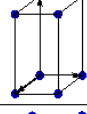
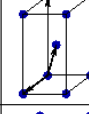
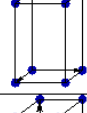
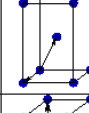
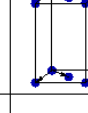
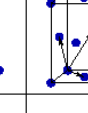
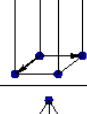
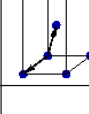
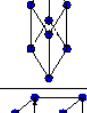
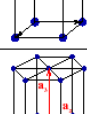
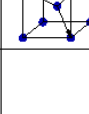

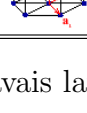
Bravais lattice	Parameters	Simple (P)	Volume centered (I)	Base centered (C)	Face centered (F)
Triclinic	$a_1 \neq a_2 \neq a_3$ $\alpha_{12} \neq \alpha_{23} \neq \alpha_{31}$				
Monoclinic	$a_1 \neq a_2 \neq a_3$ $\alpha_{23} = \alpha_{31} = 90^\circ$ $\alpha_{12} \neq 90^\circ$				
Orthorhombic	$a_1 \neq a_2 \neq a_3$ $\alpha_{12} = \alpha_{23} = \alpha_{31} = 90^\circ$				
Tetragonal	$a_1 = a_2 \neq a_3$ $\alpha_{12} = \alpha_{23} = \alpha_{31} = 90^\circ$				
Trigonal	$a_1 = a_2 = a_3$ $\alpha_{12} = \alpha_{23} = \alpha_{31} < 120^\circ$				
Cubic	$a_1 = a_2 = a_3$ $\alpha_{12} = \alpha_{23} = \alpha_{31} = 90^\circ$				
Hexagonal	$a_1 = a_2 \neq a_3$ $\alpha_{12} = 120^\circ$ $\alpha_{23} = \alpha_{31} = 90^\circ$				

Figure 3.3: The fourteen Bravais lattices in three dimensions [5].

There are 230 crystallographic space groups in three-dimensional space and they are illustrated in appendix A.

3.1.2 The reciprocal lattice and Brillouin zone

With the periodicity of a crystal lattice, any physical quantity $q(\mathbf{r})$ is also periodic so that we can expand in a Fourier series $q(\mathbf{r}) = \sum_{\mathbf{G}} \alpha_{\mathbf{G}} e^{i\mathbf{G}\mathbf{r}}$ with $\mathbf{G} = m_1\mathbf{a}^* + m_2\mathbf{b}^* + m_3\mathbf{c}^*$. The m_i are integers, and \mathbf{a}^* , \mathbf{b}^* , \mathbf{c}^* span the so-called reciprocal space. These reciprocal primitive lattice vectors are defined by

$$\mathbf{a}^* = \frac{2\pi(\mathbf{b} \times \mathbf{c})}{|\mathbf{a} \cdot (\mathbf{b} \times \mathbf{c})|}, \quad \mathbf{b}^* = \frac{2\pi(\mathbf{c} \times \mathbf{a})}{|\mathbf{a} \cdot (\mathbf{b} \times \mathbf{c})|}, \quad \mathbf{c}^* = \frac{2\pi(\mathbf{a} \times \mathbf{b})}{|\mathbf{a} \cdot (\mathbf{b} \times \mathbf{c})|} \quad (3.3)$$

with $\mathbf{a}^* \cdot \mathbf{a} = \mathbf{b}^* \cdot \mathbf{b} = \mathbf{c}^* \cdot \mathbf{c} = 2\pi$ and $\mathbf{a}^* \cdot \mathbf{b} = \mathbf{a}^* \cdot \mathbf{c} = \mathbf{b}^* \cdot \mathbf{c} = \dots = 0$, and the volume of the primitive lattice, Brillouin zone, is given by $V_{BZ} = |\mathbf{a}^* \cdot (\mathbf{b}^* \times \mathbf{c}^*)| = \frac{(2\pi)^3}{|\mathbf{a} \cdot (\mathbf{b} \times \mathbf{c})|} = \frac{(2\pi)^3}{V_{cell}}$. The Wigner-Seitz cell in the reciprocal lattice is called the first Brillouin zone, and as is expected, it has all properties of the lattice.

²The expression $V_{BZ} = \frac{(2\pi)^3}{V_{cell}}$ tells us that the larger the real primitive cell, the smaller the reciprocal primitive cell

The reciprocal lattice of a simple cubic lattice is also a simple cubic lattice, for hexagonal lattice is also hexagonal although rotated with respect to the crystal lattice. The bcc and fcc lattices are reciprocal to one another[19].

The product of \mathbf{T} , in real space, and \mathbf{G} , in reciprocal space, gives

$$\mathbf{T} \cdot \mathbf{G} = 2\pi l, \quad l = n_1 m_1 + n_2 m_2 + n_3 m_3 \quad (3.4)$$

where, as n_i and m_i are integers then, l is always integer.

We can define a function $f(\mathbf{G})$, in reciprocal lattice, which reproduces the periodicity of a periodic function, $f(\mathbf{r})$, in real lattice, by Fourier transformation

$$f(\mathbf{G}) = \frac{1}{V_{cell}} \int_{V_{cell}} d\mathbf{r} f(\mathbf{r}) \exp(i\mathbf{G} \cdot \mathbf{r}) \quad (3.5)$$

The symmetry operations are helpful in calculating and analyzing the physical properties of a crystal. By these operations, we can reduce the volume in the reciprocal space (to irreducible Brillouin zone or a fraction of the Brillouin zone)[2]. There are high-symmetry points for each of the 14 Bravais lattices, see Table 3.3. Figure 3.4 shows these high-symmetry points for two of them.

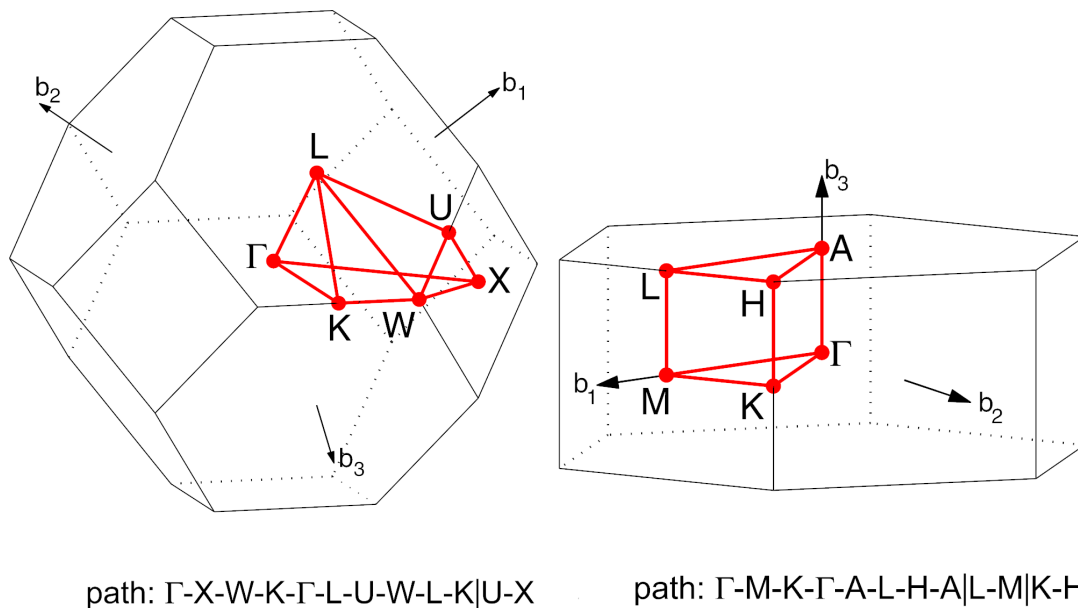


Figure 3.4: Brillouin zone and high symmetry path for FCC, on the left, and Hexagonal, on the right, structures with $b_1 \equiv a^*$, $b_2 \equiv b^*$, $b_3 \equiv c^*$ (adapted from [6]).

3.1.3 Bloch's theorem

Bloch's theorem tells us how translation symmetry affects the wavefunctions in the crystal. This theorem states that the eigenfunctions, $\psi(\mathbf{r})$, of a single-particle Hamiltonian $H = -\frac{1}{2}\nabla^2 + V(\mathbf{r})$ with a periodic potential $V(\mathbf{r}) = V(\mathbf{r} + \mathbf{T})$, for all $\mathbf{T} = n_1 \mathbf{a} + n_2 \mathbf{b} + n_3 \mathbf{c}$, can be chosen to have the form

$$\psi_{n\mathbf{k}}(\mathbf{r}) = u_{n\mathbf{k}}(\mathbf{r}) \exp(i\mathbf{k} \cdot \mathbf{r}) \quad (3.6)$$

whit $u_{n\mathbf{k}}(\mathbf{r})$ preserving the periodicity $u_{n\mathbf{k}}(\mathbf{r}) = u_{n\mathbf{k}}(\mathbf{r} + \mathbf{T})$. $u_{n\mathbf{k}}(\mathbf{r})$ is defined as $u_{n\mathbf{k}}(\mathbf{r}) = \frac{1}{\sqrt{V_{BZ}}} \sum_{\mathbf{G}} c_{n\mathbf{k}+\mathbf{G}} e^{i\mathbf{G}\mathbf{r}}$ with the Fourier coefficients specifying the form that the wavefunction $\psi_{n\mathbf{k}}(\mathbf{r})$ will take[34].

Using the Born-Von Karman condition, $\psi_{n\mathbf{k}}(\mathbf{r}) = \psi_{n\mathbf{k}}(\mathbf{r} + N_i \mathbf{a}_i)$, with \mathbf{a}_i the three primitive vectors, N_i the unit cells number for each direction, and $N = N_1 \cdot N_2 \cdot N_3$ the total number of the primitive unit cells in the crystal, we get

$$\mathbf{k} = \sum_{i=1}^3 \frac{m_i}{N_i} \mathbf{b}_i^* \quad (3.7)$$

as the Bloch wavevectors allowed with $\mathbf{b}_i^* = \mathbf{a}^*, \mathbf{b}^*, \dots$, $m_i = 0, 1, 2, \dots$, and we can determine the volume of the parallelepiped with edges $\frac{\mathbf{b}_1^*}{N_1}, \frac{\mathbf{b}_2^*}{N_2}$ and $\frac{\mathbf{b}_3^*}{N_3}$ which is actually the volume, $\Delta\mathbf{k}$, of \mathbf{k} -space per allowed \mathbf{k} as

$$\Delta\mathbf{k} = \frac{\mathbf{b}_1^*}{N_1} \cdot \left(\frac{\mathbf{b}_2^*}{N_2} \times \frac{\mathbf{b}_3^*}{N_3} \right) = \frac{V_{BZ}}{N} \quad (3.8)$$

The equation 3.8 shows that the Brillouin zone always contains the same number of \mathbf{k} as the number of the primitive unit cells in the crystal[34]. In figure 3.4, the coordinates of higher symmetry \mathbf{k} -points are given in fractions of b_1, b_2 and b_3 ³ [6].

3.1.4 Band structure and density of states

In a periodic potential, equation 3.6 tells us that, for a given n , there exists a family of solutions, one for each \mathbf{k} . Each family is called a band and each member has energy $E_{n\mathbf{k}}$ which depends on \mathbf{k} 's. Thus, we have that

$$H\psi_{n\mathbf{k}}(\mathbf{r}) = E_{n\mathbf{k}}\psi_{n\mathbf{k}}(\mathbf{r})$$

As the electrons can have spin up or spin down, each band may have just two times the number of primitive cells in the crystal. There exist energy gaps where there are no eigenstates for any n [34][19].

The density of states tells us how many states exist in a range of energy in a system, and is given as

$$g(E) = \frac{1}{N_k} \sum_{n,\mathbf{k}} \delta(\varepsilon_{n,\mathbf{k}} - E) = \frac{V_{cell}}{(2\pi)^3} \sum_n \int_{BZ} d\mathbf{k} \delta(\varepsilon_{n,\mathbf{k}} - E) \quad (3.9)$$

with N_k the number of \mathbf{k} values in the Brillouin zone which is indeed the total number of unit cells in a material, and V_{cell} is the volume of a primitive cell in real space.

3.1.5 Integrals in k-space and special k-points

For properties such as the number of electrons in bands, the total energies, etc, we must make summations over the states labeled by \mathbf{k} :

$$\langle f_n \rangle = \frac{1}{V_{BZ}} \int_{BZ} d\mathbf{k} f_n(\mathbf{k}) = \frac{V_{cell}}{(2\pi)^3} \int_{BZ} d\mathbf{k} f_n(\mathbf{k}) \quad (3.10)$$

³The Brillouin zone for all other structures can be found in[6]

But there is a simplification: using only few \mathbf{k} values in the irreducible part of the Brillouin zone, we can obtain an excellent approximation to the sum 3.11[2][19]. The most used method is the Monkhorst-Pack method which leads to a uniform set of points determined by the sequence of numbers

$$u_r = \frac{2r - q - 1}{2q} \quad (3.11)$$

with q an integer that determines the number of the special points and u_r defines then the \mathbf{k} points given as

$$\mathbf{k}_{prs} = u_p \mathbf{b}_1 + u_r \mathbf{b}_2 + u_s \mathbf{b}_3 \quad (3.12)$$

and using the symmetries of the crystal, $\langle f_n \rangle$ has the form

$$\langle f_n \rangle = \sum_{\mathbf{k}}^{IBZ} w_{\mathbf{k}} f_n(\mathbf{k}) \quad (3.13)$$

with $w_{\mathbf{k}}$ defining the total number of distinguishable \mathbf{k} points related by symmetry to the given point in the irreducible Brillouin zone (IBZ) divided by the total number of points N_k [35][19].

3.2 Lattice vibrations and phonons

The ions in crystalline materials are vibrating around their equilibrium position. These vibrations contribute to the physical properties, properties such as the superconductivity of the materials. Because of these oscillations, we expand the potential energy of the system until the second term and, by the equilibrium criterion, the linear term is equal to zero so that we have the harmonic approximation

$$U = U_0 + \frac{1}{2} \sum_{\alpha, \beta=x,y,z} \sum_{i,j} \sum_{m,n} u_{i,m}^{\alpha} D_{\alpha\beta}^{ij,mn} u_{j,n}^{\beta} \quad (3.14)$$

with the force constant between ions i and j in the cells m and n , respectively, and in $\alpha\beta$ direction, given by

$$D_{\alpha\beta}^{ij,mn} = \frac{\partial^2 U}{\partial u_{i,m}^{\alpha} \partial u_{j,n}^{\beta}} \quad (3.15)$$

3.2.1 One-dimensional diatomic lattice

We consider the one-dimensional diatomic case, figure 3.5, whose generalization to a three-dimensional case and with a general basis is straightforward. Consider a lattice with a basis of two ions, the ions with masses m_1 and m_2 , with the label 1 and 2, respectively, and these ions are harmonically oscillating around their equilibrium positions.

The index n represents the order of the ion on the chain. In this case, the system's potential energy has the form of the second term in equation 3.14 in one direction.

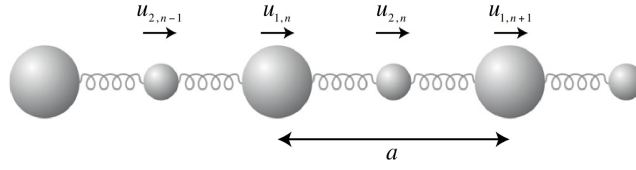


Figure 3.5: Simple diatomic chain model, with atoms of different mass connected by harmonic forces that are of equal strength between all nearest-neighbour atom pairs[7].

Considering the interaction between the neighboring ions and, as a starting point, only two ions, we have the forces acting on each one given as

$$\begin{aligned} m_1 \frac{d^2 u_{1,n}}{dt^2} &= -\frac{\partial U}{\partial u_{1,n}} = -D(u_{1,n} - u_{2,n}) - D(u_{1,n} - u_{2,n-1}) = -D(2u_{1,n} - u_{2,n} - u_{2,n-1}) \\ m_2 \frac{d^2 u_{2,n}}{dt^2} &= -\frac{\partial U}{\partial u_{2,n}} = -D(u_{2,n} - u_{1,n}) - D(u_{2,n} - u_{1,n+1}) = -D(2u_{2,n} - u_{1,n} - u_{1,n+1}) \end{aligned} \quad (3.16)$$

Equations 3.16 are second-order differential equations that admit solutions (traveling waves) that, in the general case (3D), are:

$$\mathbf{u}_i^\alpha(\mathbf{r}_\alpha, t) = \mathbf{A}_i^\alpha \exp i(\mathbf{k}^\alpha \mathbf{r}_\alpha - \omega(\mathbf{k})t) \quad (3.17)$$

with \mathbf{k} the wavevector and $\omega(\mathbf{k})$ the angular frequency.

For the case of one-dimensional diatomic lattice, we have

$$u_{1,n} = A_1 \exp i(kna - \omega t), u_{2,n} = A_2 \exp i(kna - \omega t) \quad (3.18)$$

Substituting equations 3.18 in 3.16, we obtain a system of two equations that can be written as

$$\omega^2 \begin{pmatrix} A_1 \\ A_2 \end{pmatrix} = \frac{1}{\sqrt{m_1 m_2}} \mathbf{D}(k) \begin{pmatrix} A_1 \\ A_2 \end{pmatrix} \quad (3.19)$$

with

$$\mathbf{D}(k) = \begin{pmatrix} 2D\sqrt{\frac{m_2}{m_1}} & -D\sqrt{\frac{m_2}{m_1}}(1 + \exp(-ika)) \\ -D\sqrt{\frac{m_1}{m_2}}(1 + \exp(ika)) & 2D\sqrt{\frac{m_1}{m_2}} \end{pmatrix} \quad (3.20)$$

We see that the solutions of our problem are solutions of the eigenvalue problem in equation 3.19, that is, solving the equation⁴

$$\det \left(\frac{1}{\sqrt{m_1 m_2}} \mathbf{D}(k) - \omega^2 \right) = 0 \quad (3.21)$$

This yields two solutions for ω^2 , which means that our dynamical equations have given two normal modes. If we introduce $A_1 = \frac{e_1}{m_1^{1/2}}$ and $A_2 = \frac{e_2}{m_2^{1/2}}$ in equation 3.19 and using as a new variables e_i we get a new dynamical matrix $\mathbf{D}(k)$ that is Hermitian⁵. That means that ω^2 are real and, if one of them or both ω^2 are negative then ω is imaginary and physically means that that point is not a minimum of the potential

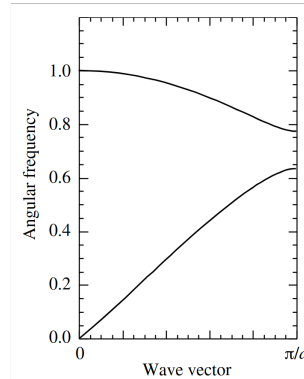


Figure 3.6: Dispersion curve of the diatomic chain model[8][7].

energy and the crystal is unstable concerning the set of displacements[7]. Figure 3.6 shows the dispersion curves for the diatomic chain. The upper curve (mode) is said optical branch and the lower curve is said acoustic branch.

3.2.2 General case

The generalizations to 3D are

- The type of solution remains the same as in equation 3.17
- equation 3.19 is $\omega^2 \mathbf{e}_i = \mathbf{D}(\mathbf{k}) \mathbf{e}_i$
- $D^{ij}(\mathbf{k}) = \sum_{\alpha, \beta=x,y,z} \sum_n \frac{1}{\sqrt{m_i m_j}} D_{\alpha\beta}^{ij,0n} \exp i[\mathbf{k}^\alpha (\mathbf{r}_{i,\alpha,0} - \mathbf{r}_{j,\alpha,n})]$

with $\mathbf{A}_i = \frac{\mathbf{e}_i}{m_i^{1/2}}$. And, for a unit cell with p atoms as the basis, there are $3p$ normal modes $\omega_s^2(\mathbf{k})$, $s = 1, 2, \dots, 3p$, with 3 acoustic modes and $3p - 3$ optical modes.

3.2.3 Phonons

There is an energy associated with the vibrations. In quantum mechanics, this energy is quantized, and the quantum is called a phonon with the energy $\hbar\omega_s(\mathbf{k})$. Thus, in 3D, a harmonic crystal has the energy

$$E = \sum_{\mathbf{k}s} (n_{\mathbf{k}s} + 1/2) \hbar\omega_s(\mathbf{k}) \quad (3.22)$$

where $n_{\mathbf{k}s}$ is the number of phonons with angular frequency $\omega_s(\mathbf{k})$. When we want to talk about lattice-lattice and lattice and external field interactions, we use phonons as the particles with momentum $\hbar\mathbf{k}$ that can be exchanged.

⁴This equation is identical to equal the equation 2.32 in three dimensions real space

⁵That means that $\mathbf{D}(k) = \mathbf{D}^\dagger(k)$

3.3 Superconductivity

Superconductivity is a state of matter exhibiting a combination of remarkable electric and magnetic properties which appear in materials when the temperature of these materials decreases below certain critical temperature (T_c). These properties are zero resistance, permanent current, perfect diamagnetism, and so on. The explanation of these and other properties are in [36] and other text books.

These properties have importance in applications from science to technology, computation, health, transport, and electricity distribution.

Today, superconductivity has been observed in a wide variety of materials (see Table 3.1) with T_c reaching up as high as 134 K[11].

Superconductor	T_c
Hg	4.2 K
Pb	7.2 K
NbGe	23 K
MgB ₂	39 K
³ He	2.5 mK
UPt ₃	0.51 K
Sr ₂ RuO ₄	0.93 K
CeCu ₂ Si ₂	0.65 K
PuCoGa ₇	18.5 K
HgBa ₂ Ca ₂ Cu ₃ O ₈	134 K
Sr _{0.5} Sm _{0.5} FeAsF	56 K

Table 3.1: Selected superconductors (adapted from [11]).

In this section, we want to talk about a mechanism from which matter can reach this state. And also we talk about the Eliashberg theory.

3.3.1 Cooper pairs and BCS theory

In a crystal, the electron-electron interaction between two electrons with energies $\varepsilon_{\mathbf{k}}$ and $\varepsilon_{\mathbf{k}'}$ is screened by the presence of other electrons and ions. So, there is a correction given as⁶

$$\frac{4\pi}{|\mathbf{k} - \mathbf{k}'|^2} \longrightarrow \frac{4\pi}{|\mathbf{k} - \mathbf{k}'|^2 + k_0^2} \left\{ 1 + \frac{\omega_{\mathbf{k},\mathbf{k}'}^2}{\omega^2 - \omega_{\mathbf{k},\mathbf{k}'}^2} \right\} \quad (3.23)$$

with $\omega = (\varepsilon_{\mathbf{k}} - \varepsilon_{\mathbf{k}'})/\hbar^2$, and $\omega_{\mathbf{k},\mathbf{k}'}$ the phonon frequency. This expression tells us that there are two regimes for electron interaction in a crystal. These regimes are associated with the energy differences between both electrons and the phonon lattice frequencies

- if $\varepsilon_{\mathbf{k}} - \varepsilon_{\mathbf{k}'} > \omega_{\mathbf{k},\mathbf{k}'}$, the second term in 3.23 is positive and the electron-electron interaction remain repulsive

⁶ k_0 is the "normal" screening of electron gas

- if $\varepsilon_{\mathbf{k}} - \varepsilon_{\mathbf{k}'} < \omega_{\mathbf{k},\mathbf{k}'}$, the second term in 3.23 is negative and larger than 1, in this situation the electrons experience an attraction

Cooper, in 1956, showed that this attraction between electrons below T_c is the core of superconductivity. That is because these pairs form bound states, the so-called Cooper pairs. This attraction is possible around the Fermi surface and, in BCS theory, between electrons with opposite momenta and spins ($\mathbf{k} \uparrow, -\mathbf{k} \downarrow$). As the equation 3.23 and the following figure show, this attraction is phonon's mediated. Particularly, the first four materials in Table 3.1 are phonon-mediated[11].

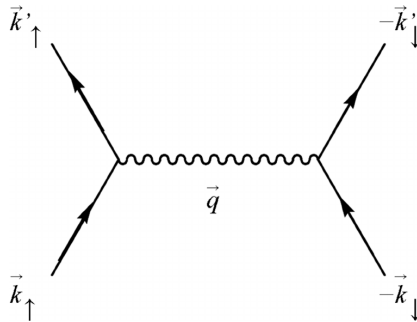


Figure 3.7: Electron-electron interaction mediated by phonon (adapted from [9]).

The interaction becomes attractive within an energy ω_D of the Fermi surface, with ω_D the Debye frequency⁷. The binding energy in BCS is given as

$$E_b = 2\omega_D \exp\left(-\frac{2}{V_0 g_F}\right) \quad (3.24)$$

with $V_0 = \text{constant} > 0$ the interaction potential and g_F the density of states at the Fermi surface.

The Cooper pair is a Bosonic particle and is the core of BCS and Eliashbergh's theories. The BCS theory considers the existence of phonons but doesn't use it explicitly in the theory. The ground state energy, at zero temperature and in \mathbf{k} -space, is given as

$$E_0^{(s)} = \sum_{\mathbf{k}} 2\varepsilon_{\mathbf{k}} |v_{\mathbf{k}}|^2 + \sum_{\mathbf{k}\mathbf{k}'} V_{\mathbf{k}\mathbf{k}'} u_{\mathbf{k}}^* u_{\mathbf{k}'}^* u_{\mathbf{k}'} v_{\mathbf{k}} \quad (3.25)$$

with the ground state wavefunction

$$\Psi_0^{(s)} = \prod_{\mathbf{k}} \{u_{\mathbf{k}} |0_{\mathbf{k}} 0_{-\mathbf{k}}\rangle + v_{\mathbf{k}} |\psi_{\mathbf{k}} \psi_{-\mathbf{k}}\rangle\} \quad (3.26)$$

where $u_{\mathbf{k}}$ and $v_{\mathbf{k}}$ must satisfy the relation

$$u_{\mathbf{k}} u_{\mathbf{k}}^* + v_{\mathbf{k}} v_{\mathbf{k}}^* = 1 \quad (3.27)$$

and $|v_{\mathbf{k}}|^2$ represents the probability that a Cooper pair of wave-vector \mathbf{k} is present in the ground state and $|u_{\mathbf{k}}|^2$ the probability that it is not. The first term in 3.26 represents unbound electron states with momenta \mathbf{k} and $-\mathbf{k}$. In equation 3.25, $\varepsilon_{\mathbf{k}}$ is

⁷In the Debye model, 1D mono-atomic case, the first Brillouin zone is replaced by a sphere of radius k_D containing all N allowed wave vectors, and $\omega_D = ck_D$ [32]

the eigenvalue of a single particle Hamiltonian ($H^{sp}\psi_{\mathbf{k}} = \varepsilon_{\mathbf{k}}\psi_{\mathbf{k}}$), and the second term results from the fact that we consider the electron-electron interaction as a process of phonon exchange.

We can show that the real superconducting ground state is given with $|u_{\mathbf{k}}|^2 = \frac{1}{2}(1 + \frac{\varepsilon_{\mathbf{k}}}{\xi_{\mathbf{k}}})$ and $|v_{\mathbf{k}}|^2 = \frac{1}{2}(1 - \frac{\varepsilon_{\mathbf{k}}}{\xi_{\mathbf{k}}})$, where $\xi_{\mathbf{k}} = \sqrt{\varepsilon_{\mathbf{k}}^2 + |\Delta_{\mathbf{k}}|^2}$ and $\Delta_{\mathbf{k}} = \sum_{\mathbf{k}'} V_{\mathbf{k}\mathbf{k}'} v_{\mathbf{k}'}^* u_{\mathbf{k}'}$. It's also possible to show that there is a gap between the normal and the superconducting states which is $E_g = 2|\Delta|$ and, in the weak coupling limit, we get that $|\Delta| = 2\omega_D \exp(-\frac{1}{V_0 g_F})$. It's very important to observe that in the BCS the interaction potential $V_{\mathbf{k}\mathbf{k}'}$ is considered as a constant $-V_0 < 0$ in the range of Debye energy.

To calculate the transition temperature, we must include the thermal effects via occupancy $n_{\mathbf{k}}$ of the single-particle state \mathbf{k} per spin unit, where we use $(1 - 2n_{\mathbf{k}})$ as the Cooper pair occupation number, $2n_{\mathbf{k}}$ for an electronic state that is not part of Cooper pair. Factor 2 is the spin degeneracy. Writing the free energy, $F^{(s)}$ of the system and considering its minimum defined by $\frac{\partial F^{(s)}}{\partial n_{\mathbf{k}}} = 0$ we get

$$n_{\mathbf{k}} = \frac{1}{1 + \exp \frac{\xi_{\mathbf{k}}}{k_B T}} \quad (3.28)$$

and the gap equation in finite temperature

$$\Delta_{\mathbf{k}} = - \sum_{\mathbf{k}'} V_{\mathbf{k}\mathbf{k}'} \frac{\Delta_{\mathbf{k}'}}{2\xi_{\mathbf{k}'}} \tanh \frac{\xi_{\mathbf{k}'}}{2k_B T} \quad (3.29)$$

which when we solve in the weak coupling limit we obtain ⁸

$$k_B T_c = 1.14 \omega_D \exp \left(-\frac{1}{g_F V_0} \right) \quad (3.30)$$

The result in the last equation shows that there exists a relation between the ion mass and the transition temperature. It is because, as we saw in section 3.2, the angular frequency of lattice vibration is proportional to $1/\sqrt{m}$, then the critical temperature is also

$$T_c \sim m^{-1/2} \quad (3.31)$$

for conventional superconductors.

3.3.2 Eliashberg theory and McMillan-Allen-Dynes formula for T_c

The Eliashberg theory is more general than the BCS theory because it includes explicitly the phonons in the theory.

A parameter that is important in the Eliashberg theory is the spectral function, also called the Eliashberg function, which describes the phonon density of states weighted by the electron-phonon interaction

$$\alpha^2 F(\omega) = \sum_{\mathbf{q}\nu} \omega_{\mathbf{q}\nu} \lambda_{\mathbf{q}\nu} \delta(\omega - \omega_{\mathbf{q}\nu}) \quad (3.32)$$

⁸here, again, we are using $\hbar = 1$

where $\lambda_{\mathbf{q}\nu}$ is the electron-phonon coupling constant for mode ν at wavevector \mathbf{q} .

Using the Eliashberg function, we can calculate ω_{ln} , called average logarithmic frequency or characteristic phonon frequency, as

$$\omega_{\text{ln}} = \exp \left[\frac{2}{\lambda} \int_0^\infty \ln(\omega) \frac{\alpha^2 F(\omega)}{\omega} d\omega \right] \quad (3.33)$$

with $\lambda = \sum_{\mathbf{q}\nu} \lambda_{\mathbf{q}\nu}$. The critical temperature, in the isotropic regime, is calculated using the McMillan-Allen-Dynes formula, for non-very strong coupling limit $\lambda < 2$ and $\mu^* < 0.15$

$$T_c = \frac{\omega_{\text{ln}}}{1.2} \exp \left[-\frac{1.04(1 + \lambda)}{\lambda - \mu^*(1 + 0.62\lambda)} \right] \quad (3.34)$$

The introduction of the Coulomb repulsive correction to electron-electron attraction is not easy so that is introduced as an empirical parameter μ^* given as $\mu^* = \frac{\mu}{1 + \mu \ln(\frac{\epsilon F}{\omega_c})}$. μ is an average electron-electron matrix element times the electronic density of states at the Fermi level and ω_c is a frequency cutoff[37][38][39][40].

Chapter 4

Methodology

In this chapter, we want to describe the procedures we used in this thesis describing. As a way to validate our results, we present the results of MgB_2 that we used as the model material. In the next chapter we talk about the results for the new materials.

The MgB_2 is a material with superconductivity experimentally observed in 2001, with $T_c = 39$ K [41]. It is also computationally simulated with a T_c of 19 K for isotropic Eliashberg theory and T_c of 39 K for the anisotropic case [42]. Another important detail is that MgB_2 is the known conventional (phonon-mediated) superconductor with its conventionality supported by isotope effect (substitution of ^{11}B by ^{10}B increases the T_c by 1 K). At normal-state, this material has low resistivity ρ (42 K) $\simeq 0.3 \mu\Omega\text{cm}$ [13].

MgB_2 is the only member of the AlB_2 family (with hexagonal space group $P6/mmm$) with a high- T_c (39 K). Other members either are not superconductors (ReB_2), or have $T_c < 10\text{K}$ (MB_2 with $M = \text{Nb, Ta, Zr}$ or Be).

The unconventional superconductors have not only one critical magnetic field but two critical magnetic fields. While the critical magnetic field in conventional superconductors destroys the superconductivity, in unconventional superconductors, increasing the applied magnetic field, firstly is observed the purely Meissner effect (exclusion of magnetic field) until reaching the first critical magnetic field (H_{c1}). After reaching H_{c1} , increasing the applied magnetic field, in unconventional superconductors is observed a mix of superconductor and normal states. That means that the magnetic field begins to penetrate the specimen. There is the second critical magnetic field (H_{c2} from which the superconductivity is destroyed).

Although MgB_2 is a conventional superconductor, it has two critical magnetic field. The high- T_c and acceptable H_{c2} (14 T) make MgB_2 a good competitor of Nb-Ti and Nb_3Sn which are the most technologically relevant superconductors in nowadays. However, some fabrication processes of MgB_2 wires for large applications are difficult because the material is brittle.

As we saw in Chapters 1 and 2, we can use DFT and DFPT to calculate properties of materials. In our case, to predict the early mentioned electronic, phononic, and superconducting properties we used the Quantum ESPRESSO (QE) software. This software is an integrated suite of open-source computer codes for electronic structure calculations of material properties using state-of-the-art electronic-structure techniques. It's based on DFT, DFPT, and pseudopotentials (norm-conserving, ultrasoft,

and projector-augmented wave) [43][44].

Generally, we used the plane wave method and pseudopotential approach for all calculus. We also used the norm-conserving pseudopotentials and LDA approximation.

The convergence energy criterion was 10^{-5} Ry/atom. We used the *vc-relax* calculation variable for the geometry optimization with the ionic relaxation (*bfgs*) [45] method.

There are two kinds of calculus, the self-consistent (SCF) and non-consistent (NSCF) calculus. The first one is exactly the procedure in 2.1 where the convergence of the charge density is imperative. The later is performed using a constant electronic density, thus being faster than a self consistent calculation. So, we can always use more \mathbf{k} -points to make a NSCF calculus easily.

For the self-consistent (SCF) and non-consistent (NSCF) calculus, we used the Monkhorst-Pack meshing method, the gaussian smearing with 0.01 Ry as the gaussian spreading for the first Brillouin zone integrations.

For the MgB_2 , the pseudopotentials used incorporate all 2s, 2p and 3s electrons for Mg and, 2s and 2p electrons for B as the valence electrons. These pseudopotentials were obtained from [46].

The steps used in our work and also the results, for instance, for MgB_2 are:

1. Convergence tests

We observed in the earlier chapter that the electrons in crystal materials are described by Bloch states, which we can expand using a plane waves basis set

$$\psi_{n\mathbf{k}}(\mathbf{r}) = u_{n\mathbf{k}}(\mathbf{r}) \exp(i\mathbf{k} \cdot \mathbf{r}) = \sum_{\mathbf{G}} \frac{1}{\sqrt{V_{BZ}}} c_{n\mathbf{k} + \mathbf{G}} \exp(i(\mathbf{k} + \mathbf{G}) \cdot \mathbf{r}) \quad (4.1)$$

where $u_{n\mathbf{k}}(\mathbf{r})$ is a function that has the same periodicity as the lattice, \mathbf{k} taking N (number of unit cells) into Brillouin zone, and the sum over reciprocal lattice vectors \mathbf{G} being infinite.

Substituting this expression in the Kohn-Sham equations 2.25, we get a set of matrix equations. However, in practice we can't do infinite sums so that we must truncate the plane waves and the \mathbf{k} -points to soft values, i.e, values that give us accurate results. For the plane wave expansion we define a kinetic energy cutoff, in atomic units,

$$E_{cut} = \frac{1}{2}(\mathbf{k} + \mathbf{G})^2 \quad (4.2)$$

meaning that the number of plane waves, N_{op} , included in the calculation scales is $N_{op} \sim E_{cut}^{3/2}$.

The way as we introduce the \mathbf{k} -points depends on the relation between the lattice parameters, and obeys the rule $N_1 : N_2 : N_3 \approx 1/|a_1| : 1/|a_2| : 1/|a_3|$. That means that if we have a structure with $a \times ma \times na$ then the grid is $k \times k/m \times k/n$. Many times these fractions are not integers, so we use the immediate integer numbers. For integrations on the Brillouin zone, we use a set of finite \mathbf{k} -point grids.

The convergence tests were performed to determine the cutoff energies and \mathbf{k} -point grids which converged the values of the total energy per atom within 10^{-5} Ry/atom.

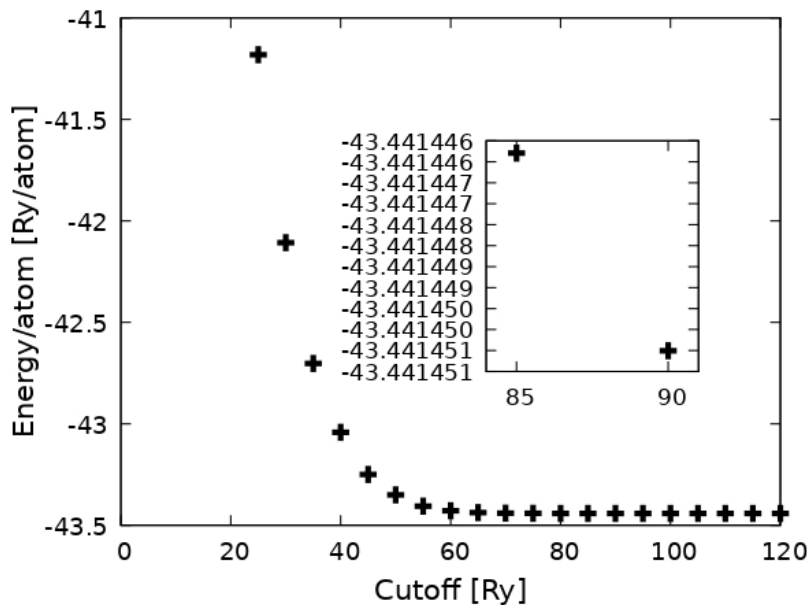


Figure 4.1: Cutoff convergence for MgB_2 .

As the figure 4.1 shows, we calculated the energy/atom for different cutoff energies and determined the point from which the energy decrease is less or equal to 10^{-5}Ry/atom . For this case, we have that the converged cutoff energy is 80 Ry. The same procedure gave converged k-point grid equal to 12.

2. Geometry optimization

A crucial step is the geometry optimization with which we determine the geometry with the minimum energy, i.e, the geometry for which the total force/atom, \mathbf{F}_I , and stress are zero. For MgB_2 we started with the experimental structure, which is hexagonal structure with its lattice vectors $\mathbf{a} = (\sqrt{3}/2, 1/2, 0)a$, $\mathbf{b} = (0, 1, 0)a$ and $\mathbf{c} = (0, 0, 1)c$. This structure has a graphite-like B_2 layer between Mg layers. Our result of the geometry optimization calculation gave the same result (hexagonal structure), figure 4.2. The results for the lattice parameters are $a = 3.036\text{\AA}$ and $c/a = 1.139$, with $c = 3.459\text{\AA}$. This is result is in agreement with previous DFT calculations [47][48][49][50].

3. Electronic band structure and density of states

After the geometry optimization, we began to calculate the electronic band structure and density of states to observe if the material is a metal or not. In the electronic structure calculation, we made SCF calculation to get wave-functions and charge density. Because we included the smearing variable in our input calculation, also we get Fermi energy which is necessary for the band calculations.

After the NSCF calculation, we made the bands' calculation for the high-symmetry paths suggested in references [6] and [51]. To get these high-symmetry paths, we used the xcrsden software [10].

With the bands' calculations, we extracted bands using the bands.x code, and, finally, we used Gnuplot [52] to the plot the graphics.

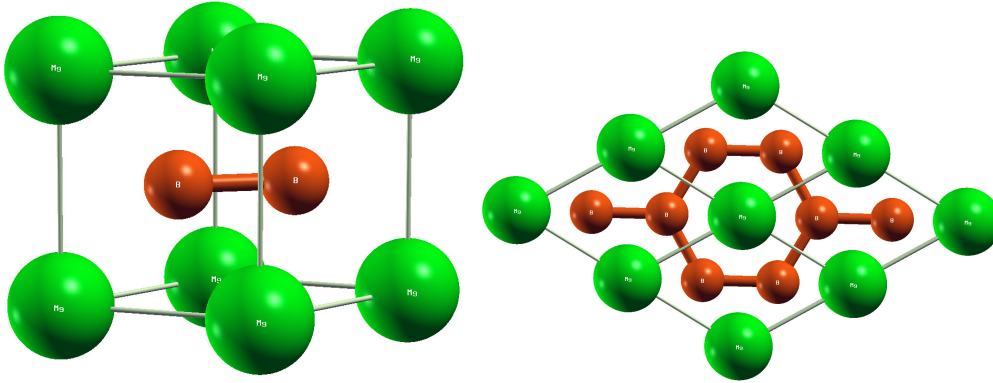


Figure 4.2: Hexagonal structure of MgB_2 . left: primitive unit cell; right: 2×2 supercell viewed from the z direction. Images obtained using xcrystden[10].

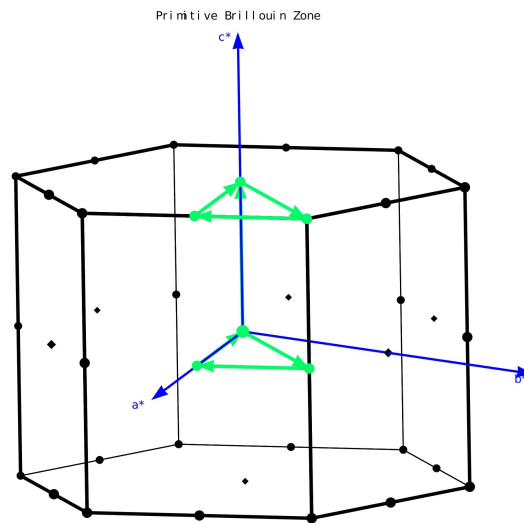


Figure 4.3: High-symmetry path, $\Gamma-M-K-\Gamma-A-L-H-A$, for hexagonal structure in xcrystden [10].

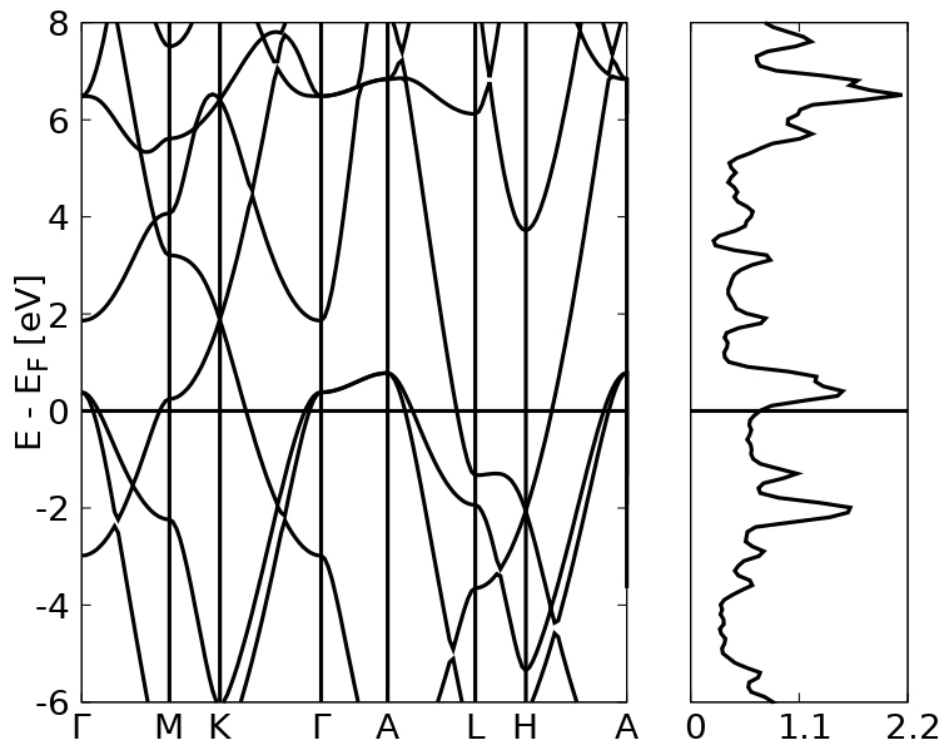
For the Density of states (DOS), we used the previous procedure for electronic band structure, only changing the occupations variable, where we used occupations = tetrahedra to obtain a soft curve and eliminate spurious around the gap caused by the smearing. To extract the DOS we used dos.x code.

For MgB_2 case we get the expected results, i.e, it's a metal[48]. The electronic band structure and DOS of MgB_2 obtained is showed in the figure 4.4.

The calculation of DOS is the last step in the electronic calculations, where the main goal was to observe if the material is or not a metal. If the material is a metal, the following steps are making the k -points convergence for that phonon calculation, the phonon spectrum and electron-phonon coupling constant calculations, and, as the last step, the critical temperature calculation.

4. k -points convergence for phonon calculations

There are two possibilities to make phonon calculations. Using the ph.x code, the calculation can be for a specific \mathbf{q} -point or a selected set of \mathbf{q} points. For

Figure 4.4: Electronic structure and DOS of MgB₂.

the calculation of phonons, the convergence test means running ph.x code for different \mathbf{q} for different \mathbf{k} -point grids and observe the frequency changes for each normal mode. We used the Γ point for that goal. We start with the converged \mathbf{k} -points from the electronic structure calculation.

Our results show that often the \mathbf{k} -point grid used in the previous calculations is sufficient. However, as a practical way for phonon calculation for a general calculation, it's necessary to select a \mathbf{k} -points grid with, if possible, at least, two dividers different from one. That is why many times we increase the converged \mathbf{k} -points to another adequate values.

$k = 12$	$k = 15$	$k = 16$
0.537049	0.538359	0.537923
0.537049	0.538359	0.537923
0.540860	0.541568	0.540591
10.449623	10.426689	10.418321
10.449623	10.426689	10.418321
12.505183	12.447760	12.502675
20.152897	17.549041	18.426109
20.15289	17.549041	18.426109
21.195794	21.297623	21.194891

Table 4.1: Frequency, in cm^{-1} , of the phonon modes of MgB₂ at Γ point for \mathbf{k} -point grids (k, k, k) with $k = 12$, $k = 15$ and $k = 16$, from left to the right.

Our calculations showed that 12x12x12 is a k-point grid sufficient for phonon calculations, as the Table 4.1 shows.

5. Obtaining the phonon spectrum, electron-phonon coupling constant, and T_c

Our result for the phonon spectrum, figure 4.5, is similar to results previously obtained by references [47][53]. As it is shown in the phonon density of states, 4.5, around 343 cm^{-1} to up begin the high contribution of boron in the lattice vibrations, while the lower contribution comes from Mg.

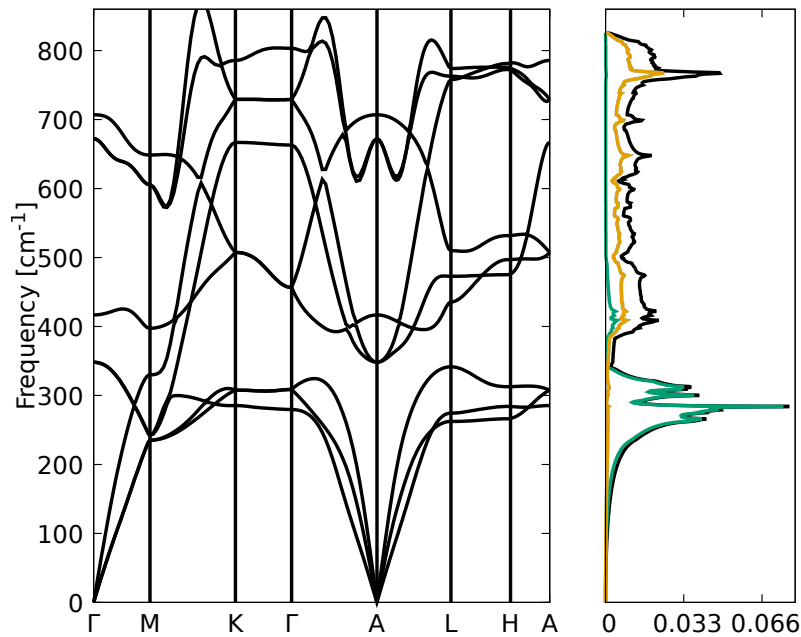


Figure 4.5: Phonon spectrum, on the left, and phonon DOS, on the right, of MgB_2 for 12x12x12 k-point grids, 6x6x6 q-point grids and $n_k = 16$. Particularly, in the phonon DOS the black graph is the total DOS, the green is the contribution of Mg and the dark-orange are the B contributions.

On the the calculation of electron-phonon coupling and T_c we must the define a plateau which is the maximum difference between two subsequent electron-phonon coupling constant. We defined the plateau being 0.007. With this plateau, we have that the coupling constant is 0.61688 and the respective T_c is 14.947 K. These results are possible to see in the figures 4.6 and 4.7 with the green lines. The defined smearing is 0.006 and ω_{in} is 746.551 K.

These results are satisfactory for us because they are close to previous DFT calculations using the McMillan-Allen-Dynes formula. That means that we can use the same steps to predict the superconducting properties of the new materials and get insights into them.

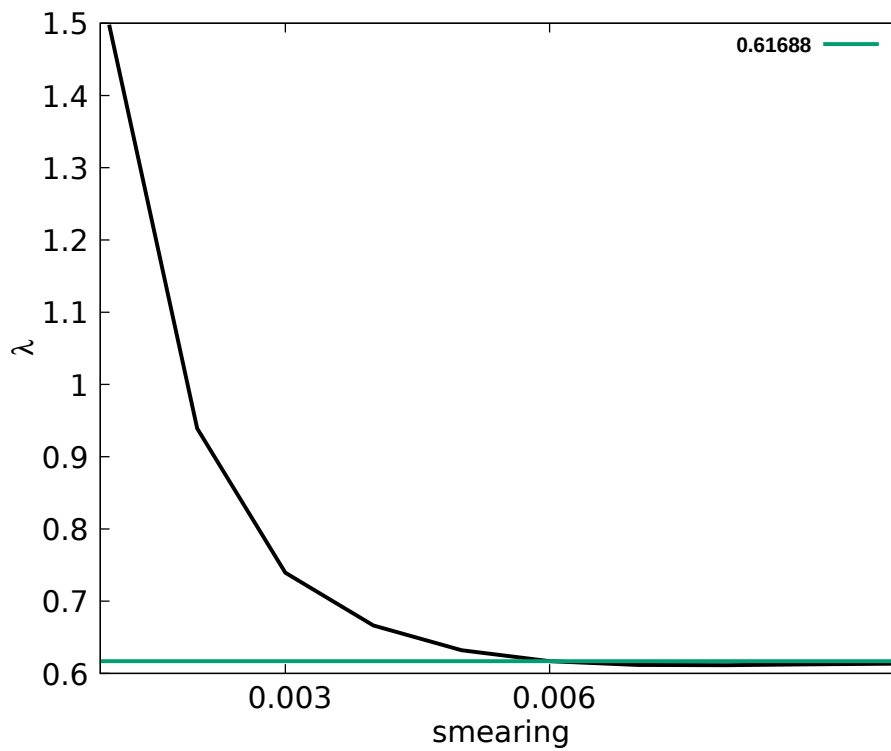


Figure 4.6: Coupling constant of MgB_2 as a function of the smearing parameter.

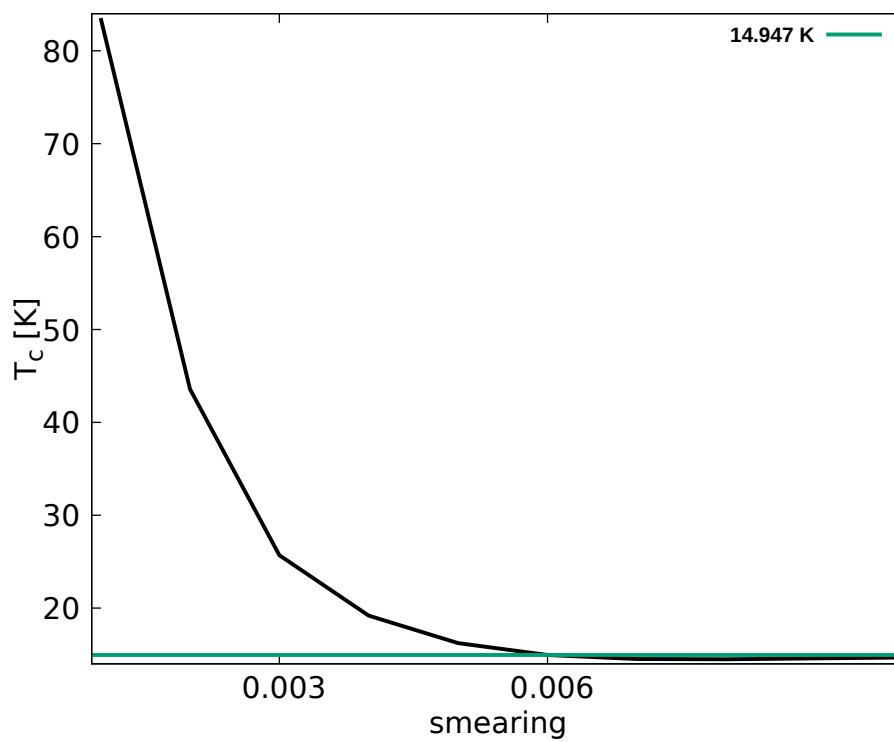


Figure 4.7: Transition temperature of MgB_2 as a function of the smearing parameter.

Chapter 5

Results

5.1 Electronic structure calculations

We studied a set of new metallic ternary materials, listed in Table 5.1, that were previously discovered by other members of our research group.

Material	Structure	SPG	Volume (<i>a.u.</i>) ³	Lattice parameters
Al ₂ Li ₂ Pd ₂	Hexagonal	P3m1	535.2	a=4.186 Å, c/a = 1.25
Al ₂ Li ₃ Pd		P-3m1	566.8	a=4.226 Å, c/a = 1.29
Al ₃ LiPd ₂		P-3m1	546.4	a=4.238 Å, c/a = 1.23
AlLi ₂ Pd ₃		P-3m1	505.4	a=4.136 Å, c/a = 1.22
AlLi ₄ Pd		P3m1	577.2	a=4.269 Å, c/a = 1.27
Al ₂ LiPd	fcc	Fm-1m	361.1	a=5.982 Å
AlLiPd ₂		Fm-3m	344.0	a=5.886 Å
Al ₄ LiPd	Trigonal	R3m	632.0	a=6.520 Å, cos(γ) = 0.790
Al ₂ Li ₂ Pd		R-3m	461.8	a=5.071 Å, cos(γ) = 0.655

Table 5.1: Resume of the crystalline information of the Al_xLi_yPd_z ternary materials.

Al₂Li₂Pd₂, Al₂Li₃Pd, Al₃LiPd₂, AlLi₂Pd₃ and AlLi₄Pd have a hexagonal structure. Their lattice parameters are indicated in Table 5.1 and their structures are shown in Figures 5.1–5.5.

Al₂LiPd and AlLiPd₂ have a fcc structure, and Al₄LiPd and Al₂Li₂Pd were found to possess trigonal R crystalline structures. Their lattice parameters are indicated in Table 5.1 and their structures are shown in Figures 5.6–5.8.

We used norm-conserving, scalar relativistic pseudopotentials taken from PSEUDO-DOJO [46]. They include all the 3s and 3p electrons of Al, all 3 electrons of Li, and all 4s, 4p, and 4d electrons of Pd.

All the hexagonal structures had total energy converged with respect to kinetic energy cutoff at 80 Ry. Although convergence with respect to the k-points grid was already attained for a coarser grid, we used a 12x12x12 grid in our calculations for all the hexagonal structures in order to get really accurate densities of states and band structures.

The electronic band structure and density of states of all the hexagonal compounds are plotted in Figures 5.9–5.13.

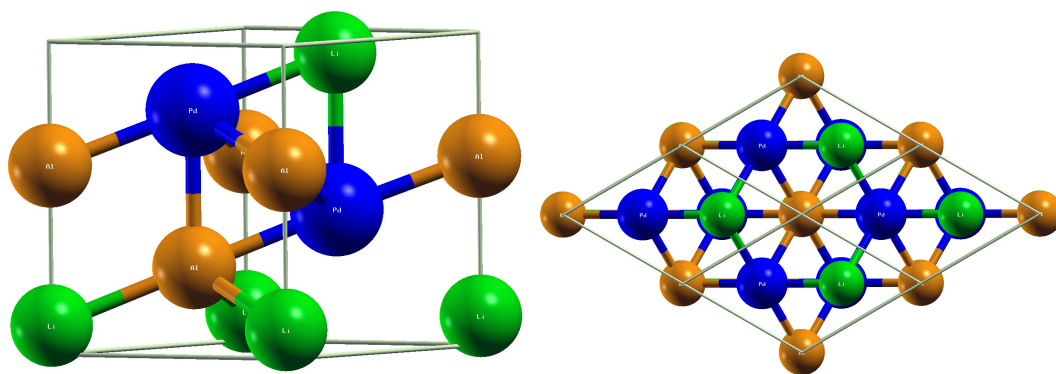


Figure 5.1: Hexagonal structure of $\text{Al}_2\text{Li}_2\text{Pd}_2$. Left: primitive unit cell; right: z direction visual with 2 unit cells in the x and y directions.

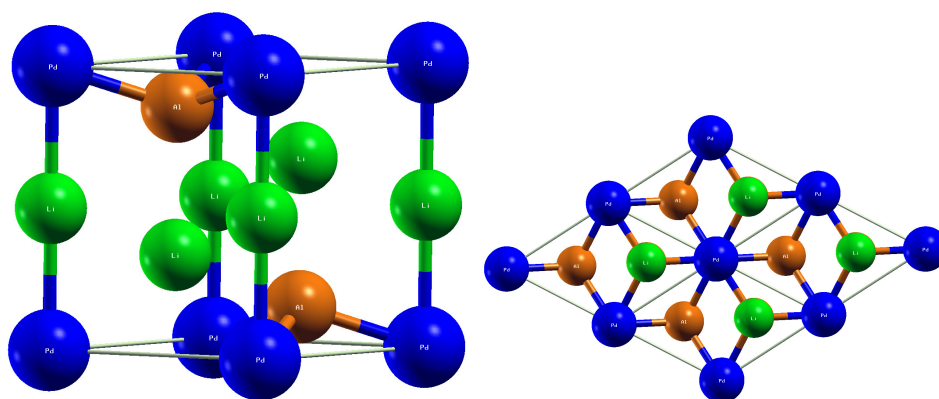


Figure 5.2: Hexagonal structure of $\text{Al}_2\text{Li}_3\text{Pd}$. Left: primitive unit cell; right: z direction visual with 2 unit cells in the x and y directions.

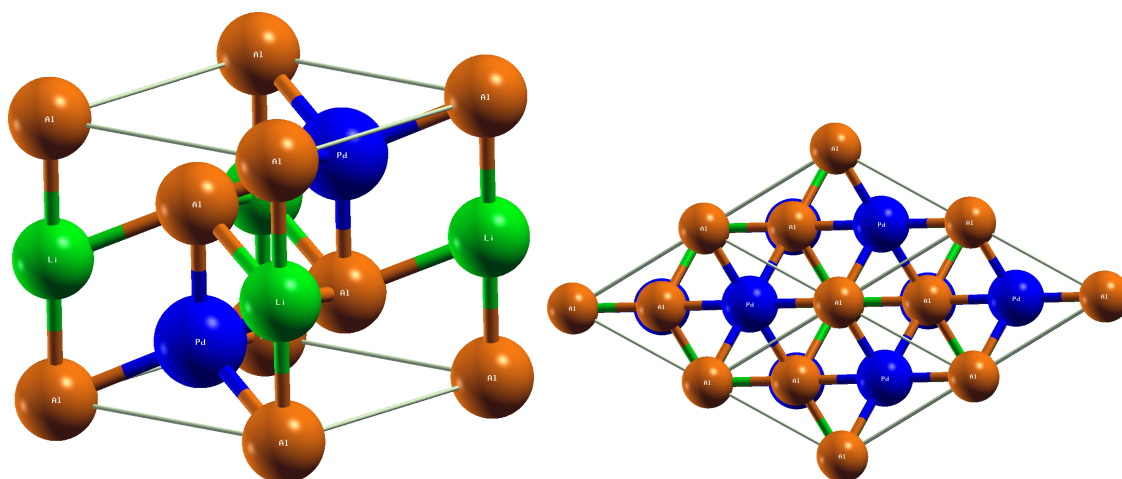


Figure 5.3: Hexagonal structure of Al_3LiPd_2 . Left: primitive unit cell; right: z direction visual with 2 unit cells in the x and y directions.

Results for the fcc structures indicated that the calculations were converged with a kinetic energy cutoff 80 Ry, as before. This was expected, as the pseudopotentials were the same. However, as the structures were different, the convergence with respect to

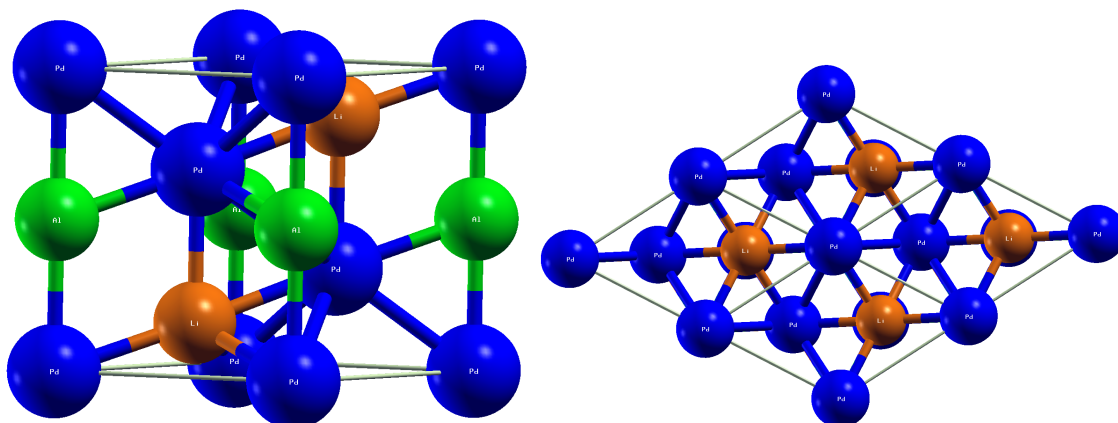


Figure 5.4: Hexagonal structure of AlLi₂Pd₃. Left: primitive unit cell; right: z direction visual with 2 unit cells in the x and y directions.

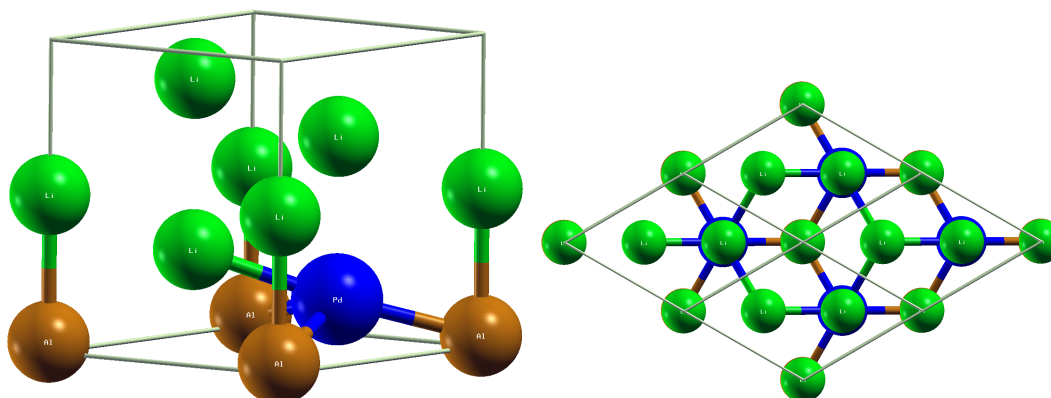


Figure 5.5: Hexagonal structure of AlLi₄Pd. Left: primitive unit cell; right: z direction visual with 2 unit cells in the x and y directions.

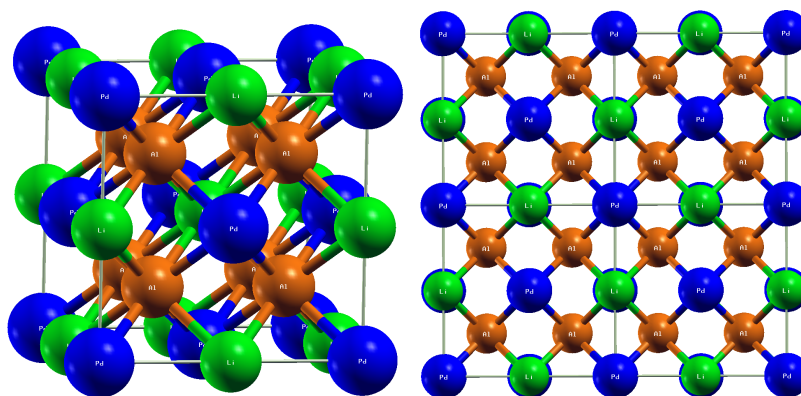


Figure 5.6: fcc structure of Al₂LiPd. Left: primitive unit cell; right: z direction visual with 2 unit cells in the x and y directions.

the k-points grid indicated the need for denser grids for the fcc structures: 15x15x15 for Al₂LiPd, and 12x12x12 for AlLiPd₂. For the trigonal R crystalline structures we used a 12x12x12 k-point grid for Al₄LiPd, and a 15x15x15 k-point grid for Al₂Li₂Pd. For the trigonal structures, convergence with respect to the kinetic energy cutoff was reached

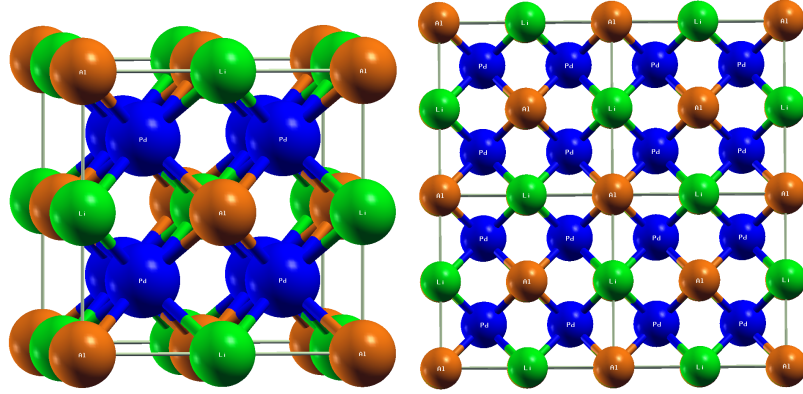


Figure 5.7: fcc structure of AlLiPd₂. Left: primitive unit cell; right: z direction visual with 2 unit cells in the x and y directions.

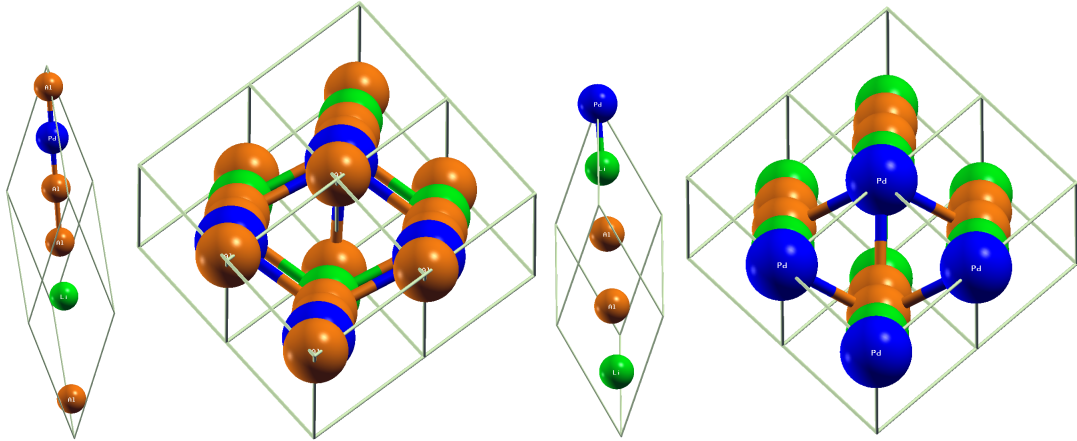


Figure 5.8: Trigonal structure of Al₄LiPd (leftmost figures) and Al₂Li₂Pd (rightmost figures). First and third figures: primitive unit cells; second and fourth figures: z direction visual with 2 unit cells in the x and y directions.

at 75 Ry and 120 Ry, respectively, although we incremented 5 Ry for the electronic band structure and density of states for both materials.

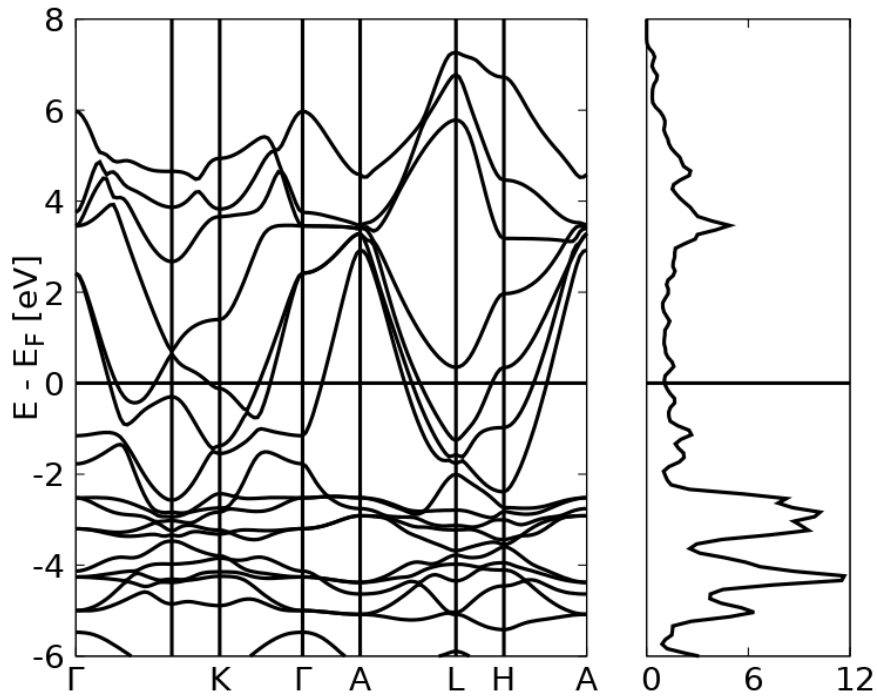
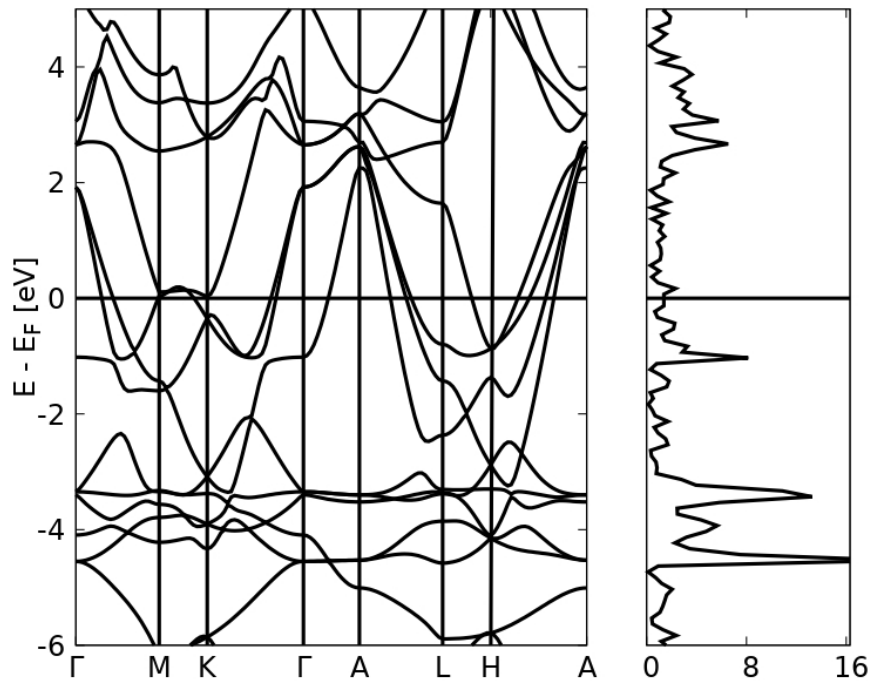
The electronic band structures and densities of states of all the last four materials are illustrated in Figures 5.14–5.17.

5.2 Phonon spectra and T_c calculations

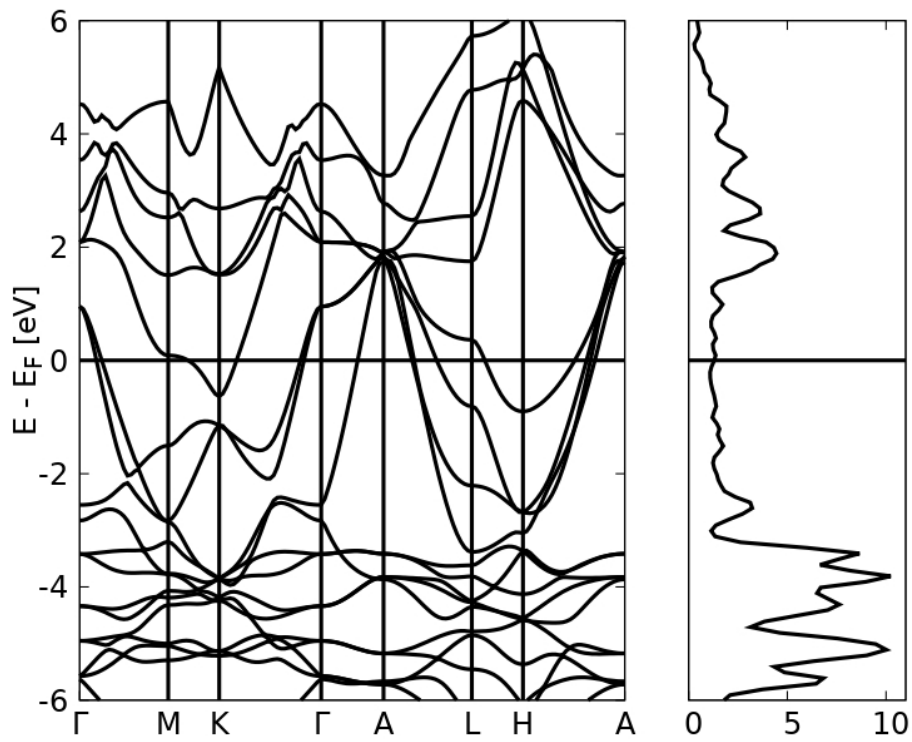
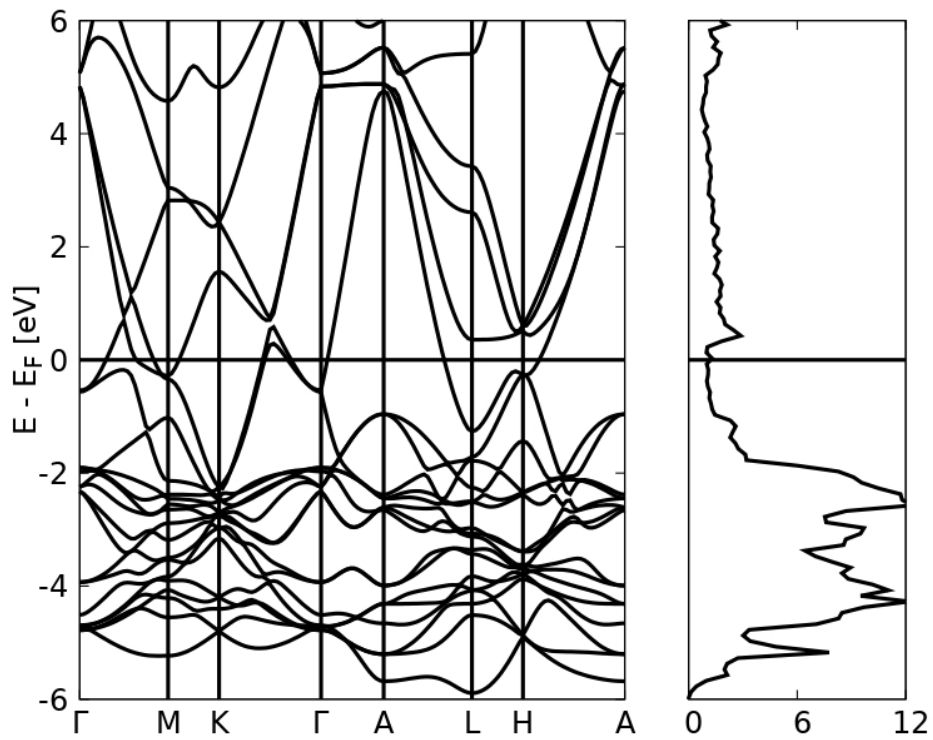
After the convergence tests and electronic structure calculations, we began with phonon spectra and T_c calculations for all materials.

5.2.1 Phonon spectra and T_c of the hexagonal structures

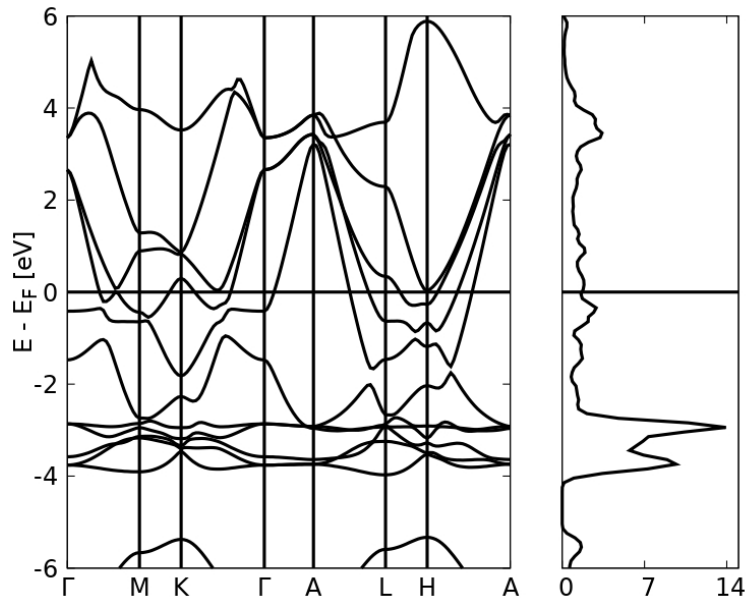
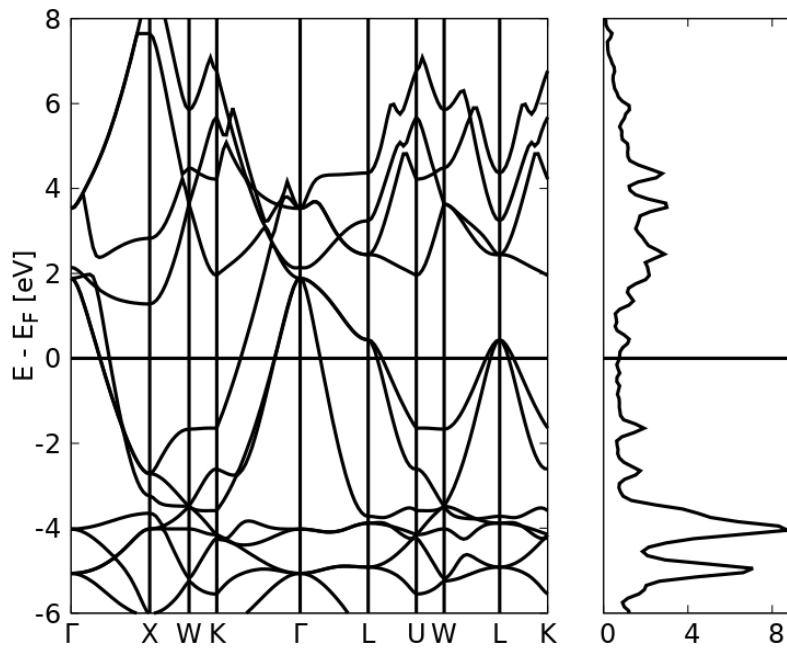
Although band structures and densities of states were very well converged with the k-points grids mentioned before, we decided to increase the grid for phonon calculations, in order to be sure that the coupling constant calculations and lambda calculations

Figure 5.9: Electronic band structure and DOS of $\text{Al}_2\text{Li}_2\text{Pd}_2$.Figure 5.10: Electronic band structure and DOS of $\text{Al}_2\text{Li}_3\text{Pd}$.

were really well converged. As the k-points grid has to be commensurate to the q-point grid for the phonon calculations, the increase in the the k-points sampling took in account that the q-grids chosen were $3 \times 3 \times 3$ for Al_3LiPd_2 , $\text{Al}_2\text{Li}_3\text{Pd}$, $\text{Al}_2\text{Li}_2\text{Pd}_2$ and AlLi_4Pd , and $6 \times 6 \times 6$ for AlLi_2Pd_3 . Therefore, we used a coarse k-grid of $15 \times 15 \times 15$,

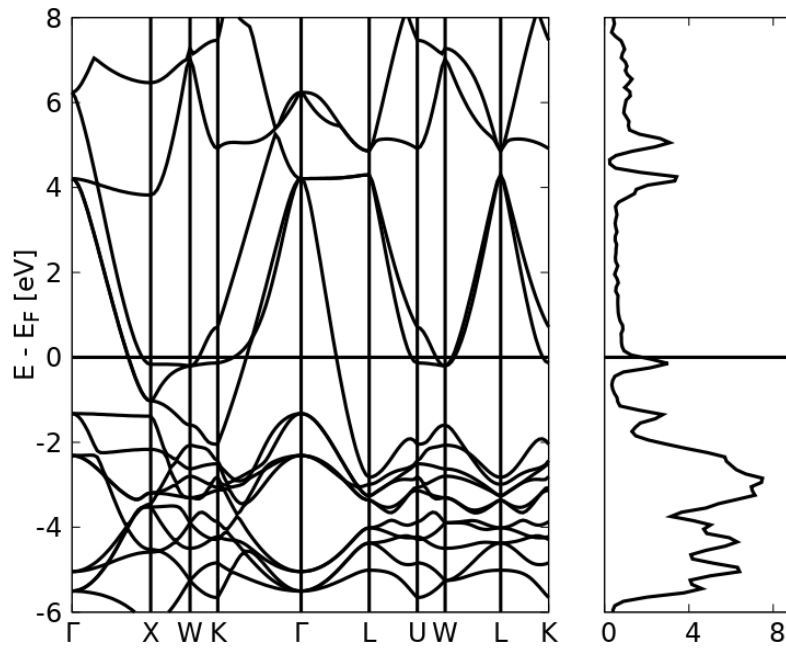
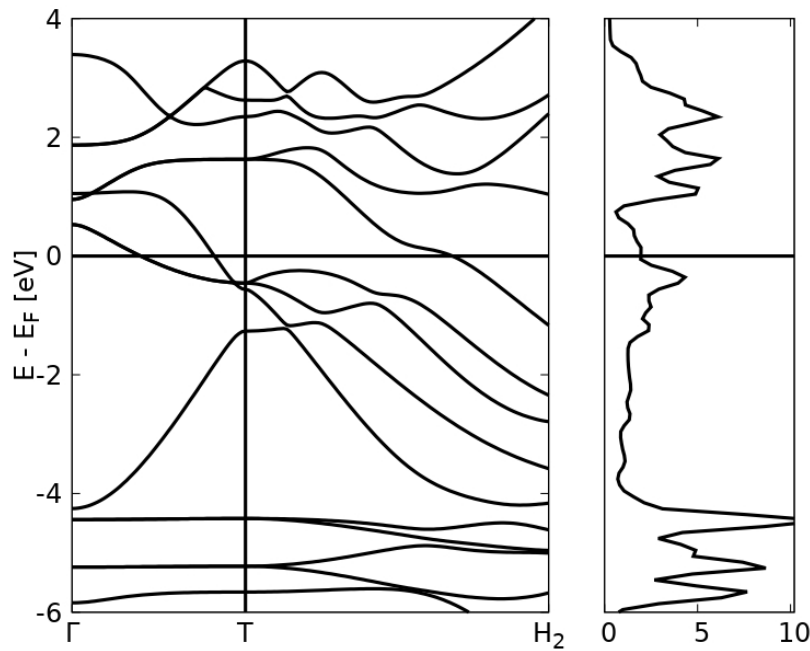
Figure 5.11: Electronic band structure and DOS of Al_3LiPd_2 .Figure 5.12: Electronic band structure and DOS of AlLi_2Pd_3 .

and a fine k-grid of $30 \times 30 \times 30$ for Al_3LiPd_2 , $12 \times 12 \times 12$ and $24 \times 24 \times 24$ for $\text{Al}_2\text{Li}_2\text{Pd}_2$ and $12 \times 12 \times 12$ and $36 \times 36 \times 36$ for $\text{Al}_2\text{Li}_3\text{Pd}$, AlLi_4Pd and AlLi_2Pd_3 . Phonon spectra and DOS


 Figure 5.13: Electronic band structure and DOS of AlLi_4Pd .

 Figure 5.14: Electronic band structure and DOS of Al_2LiPd .

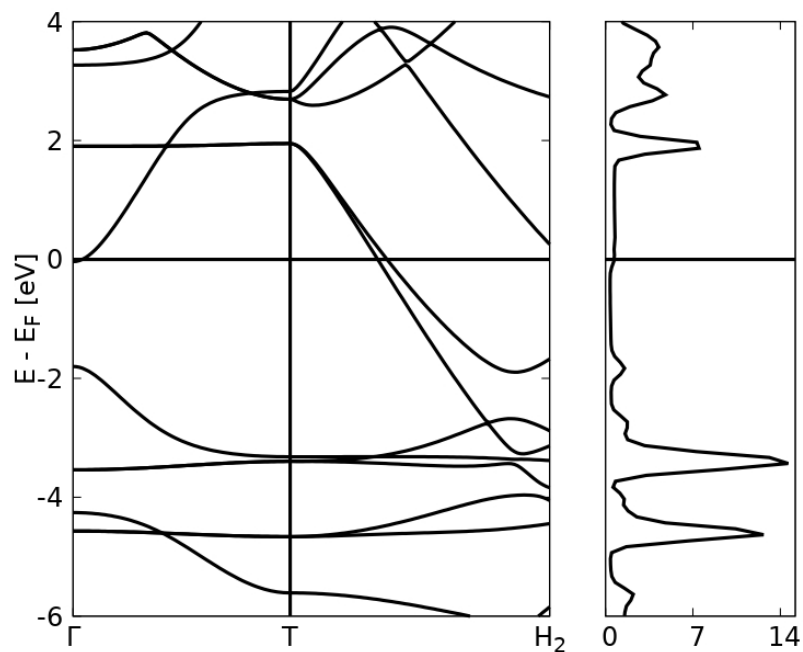
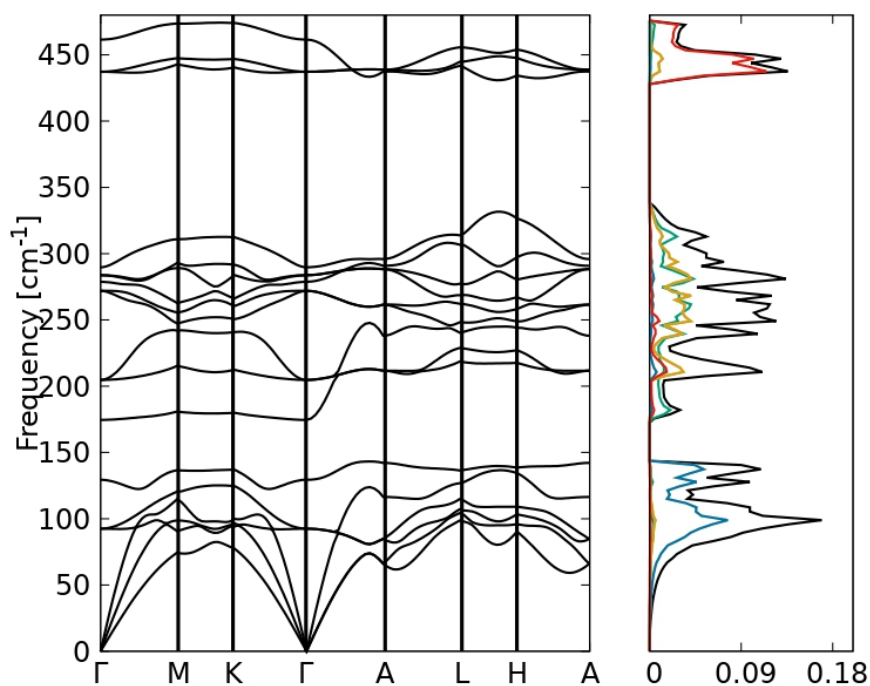
of phonons are presented in figures 5.18–5.22.

The coupling and transition temperatures are as follows: 0.34 and 0.15 K for $\text{Al}_2\text{Li}_2\text{Pd}_2$, 0.34 and 0.17 K for $\text{Al}_2\text{Li}_3\text{Pd}$, 0.37 and 0.27 K for Al_3LiPd_2 , 0.13 and 0.0 K for AlLi_2Pd_3 , and 0.55 and 2.43 K for AlLi_4Pd .

Figure 5.15: Electronic band structure and DOS of AlLiPd₂.Figure 5.16: Electronic band structure and DOS of Al₄LiPd.

5.2.2 Phonon spectra and Tc of the fcc structures

For materials with fcc structure, we used for Al₂LiPd a coarse k-point grid with 15x15x15 points and a denser k-point grid with 30x30x30 points. The q-points grid for the phonon, lambda, and Tc calculations was a 5x5x5 grid. For AlLiPd₂ we used 16x16x16 and 32x32x32 k-point grids and a 4x4x4 q-point grid. The phonon spectra and DOS of phonons of this set of materials are in figures 5.23 and 5.24.

Figure 5.17: Electronic band structure and DOS of $\text{Al}_2\text{Li}_2\text{Pd}$.Figure 5.18: Phonon spectrum and density of states of phonon of Al_3LiPd_2 , with blue color for Pd contribution, yellow and green for Al contribution, and finally, red color for Li contribution.

With these data we obtained λ and T_c equal to 0.27 and 0.008 K for Al_2LiPd and 0.21 and 0.0 K for AlLiPd_2 .

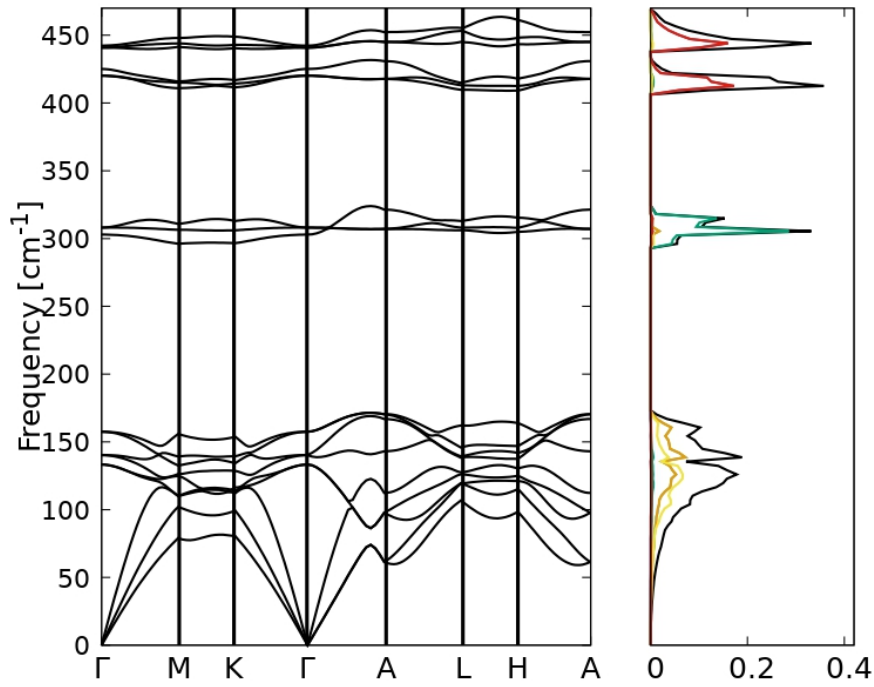


Figure 5.19: Phonon spectrum and density of states of phonon of AlLi_2Pd_3 , with yellow and orange for Pd contribution, green for Al, and finally, red color for Li contribution.

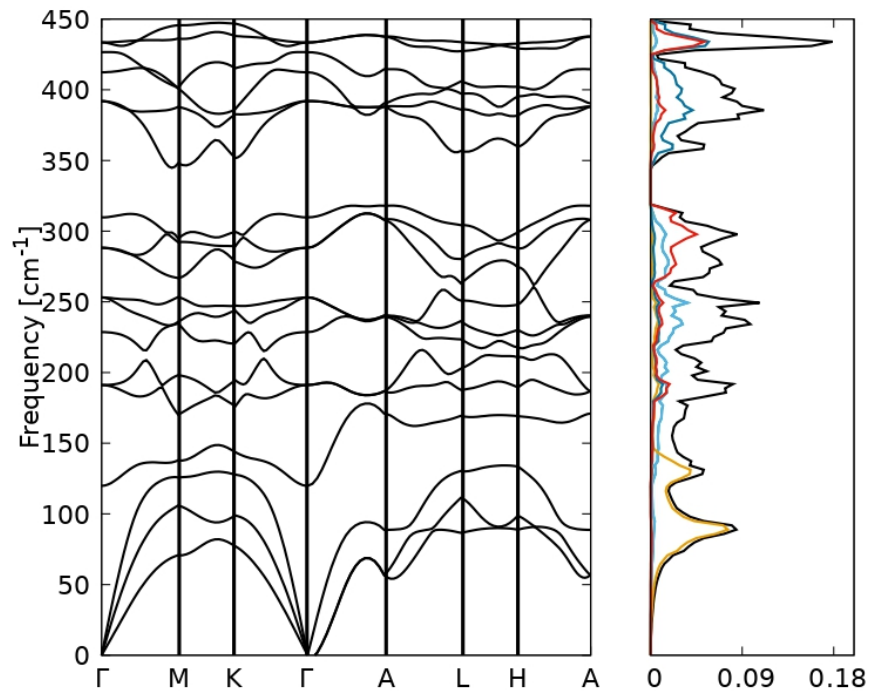


Figure 5.20: Phonon spectrum and density of states of phonon of $\text{Al}_2\text{Li}_3\text{Pd}$, with yellow color for Pd contribution, red for Al contribution, and finally, blue color for Li contribution.

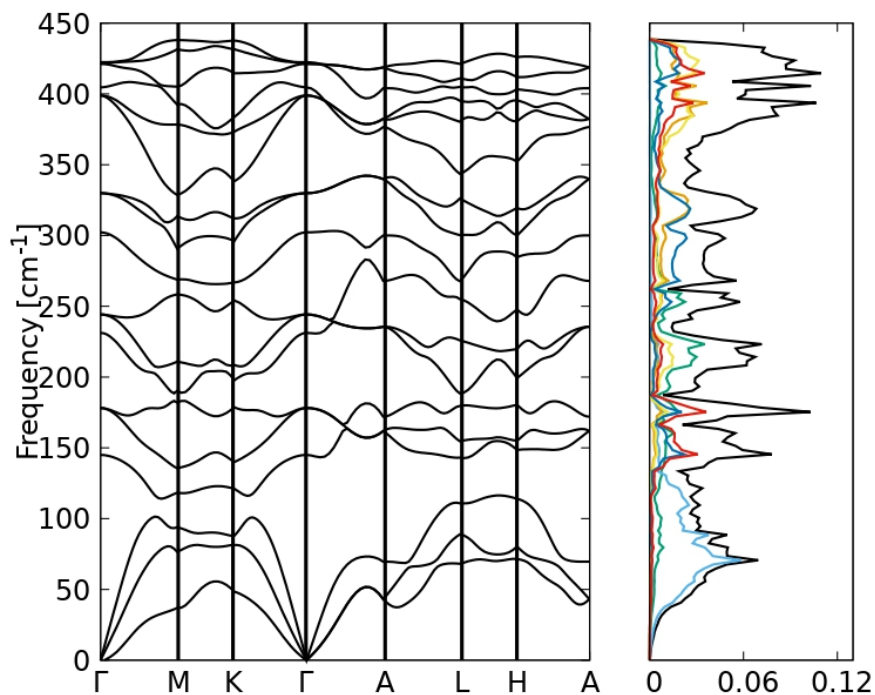


Figure 5.21: Phonon spectrum and density of states of phonon of AlLi_4Pd , with blue color for Pd contribution, dark blue for Al contribution, and finally, other colors for Li contribution.

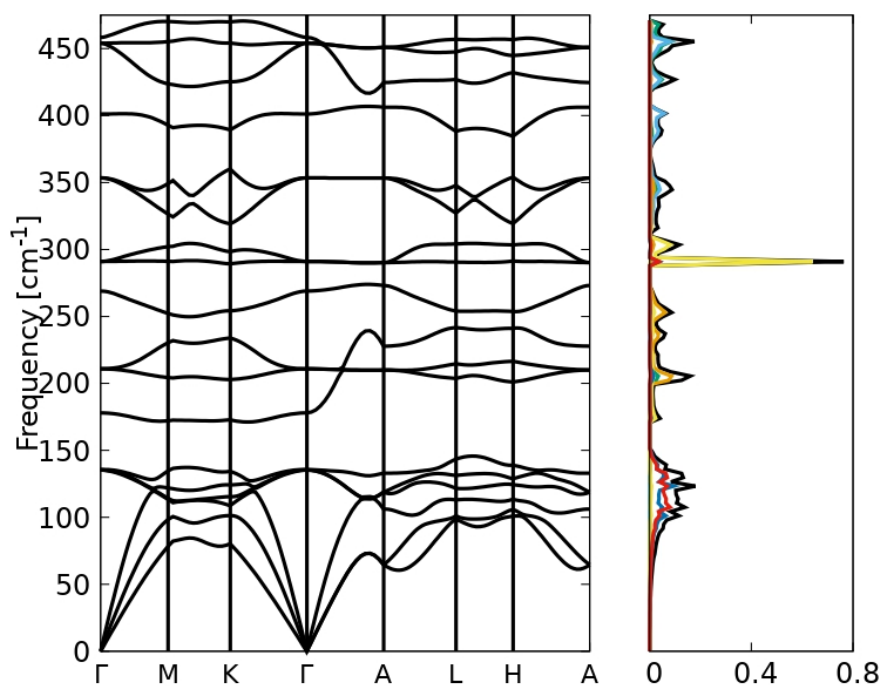


Figure 5.22: Phonon spectrum and density of states of phonon of $\text{Al}_2\text{Li}_2\text{Pd}_2$, with red color for Pd contribution, yellow and orange for Al contribution, and finally, blue color for Li contribution.

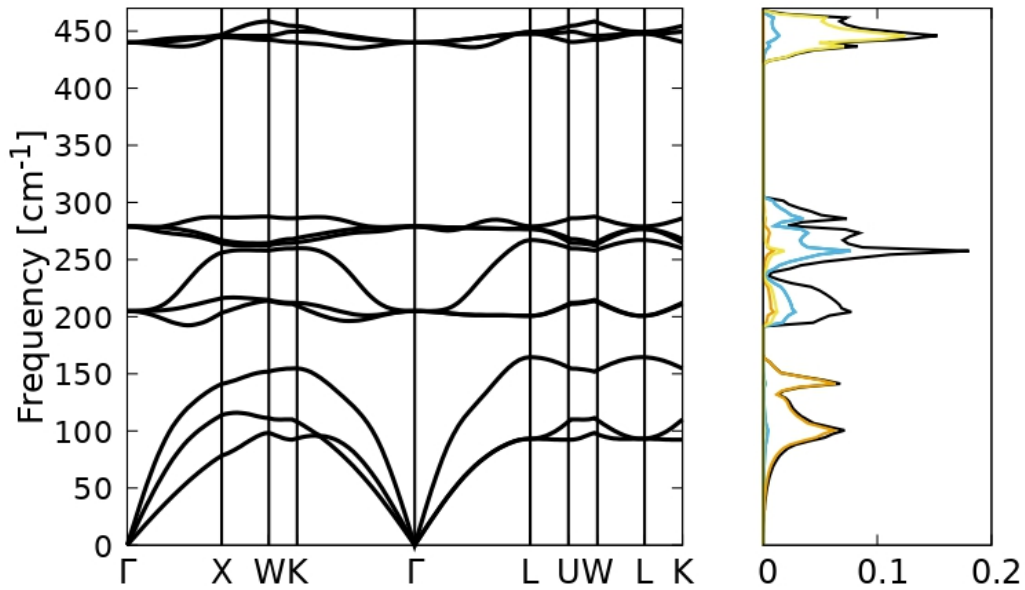


Figure 5.23: Phonon spectrum and density of states of phonon of Al_2LiPd , with orange color for Pd contribution, blue for Al contribution, and finally, yellow color for Li contribution.

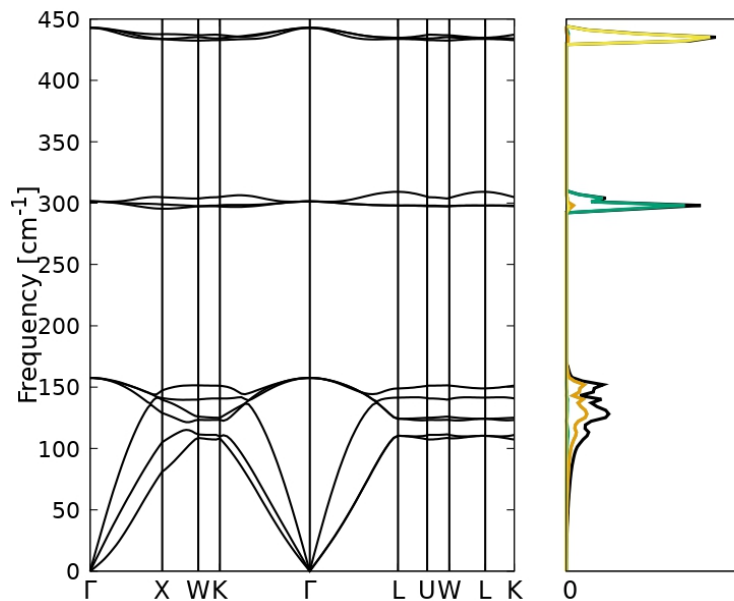


Figure 5.24: Phonon spectrum and density of states of phonon of AlLiPd_2 , with orange color for Pd contribution, blue for Al contribution, and finally, yellow color for Li contribution.

5.2.3 Phonon spectra and T_c of the Trigonal R (3 fold axis c) structures

The phonon spectra of trigonal structures are given in figures 5.25 and 5.26.

For these materials, we used for Al_4LiPd a $36 \times 36 \times 36$ and $12 \times 12 \times 12$ fine and coarse

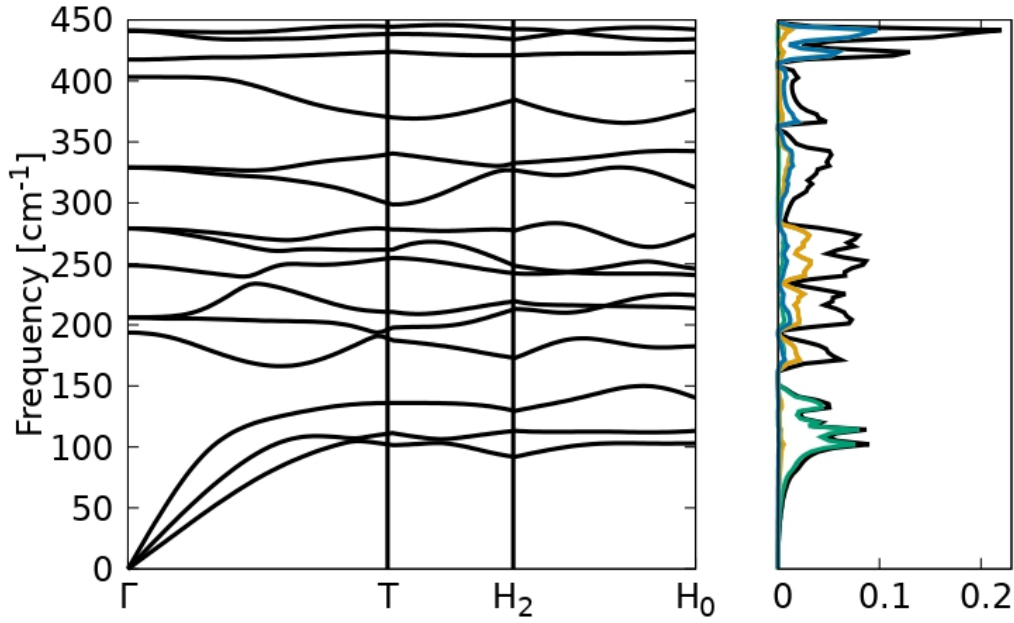


Figure 5.25: Phonon spectrum and density of states of phonon of $\text{Al}_2\text{Li}_2\text{Pd}$, with green color for Pd contribution, grey for Al contribution, and finally, blue color for Li contribution.

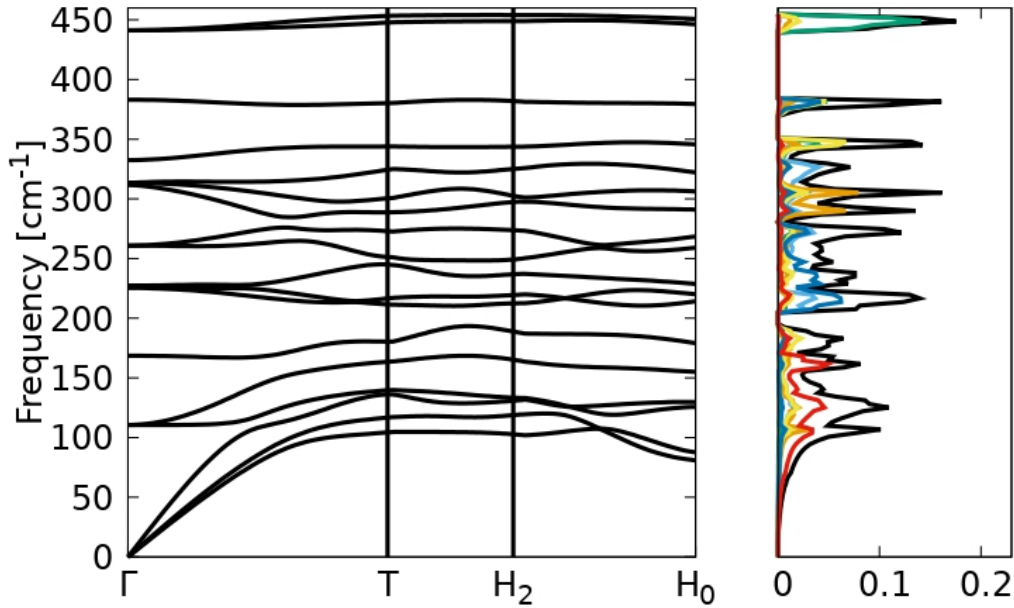


Figure 5.26: Phonon spectrum and density of states of phonon of Al_4LiPd , with red color for Pd contribution, blue, yellow and grey for Al contribution, and finally, green color for Li contribution.

k-point grids, respectively. For phonons, we used a $3 \times 3 \times 3$ q-point grid, as well as for lambda, and Tc calculations. For $\text{Al}_2\text{Li}_2\text{Pd}$ we used $15 \times 15 \times 15$ and $30 \times 30 \times 30$ k-point grids and a $5 \times 5 \times 5$ q-point grid. With these data, we obtained lambda and Tc equal to 0.21 and 0.00 K for Al_4LiPd , and 0.31 and 0.059 K for $\text{Al}_2\text{Li}_2\text{Pd}$.

5.2.4 Summary

The following table summarizes all information about the calculations for all $\text{Al}_x\text{Li}_y\text{Pd}_z$ ternary materials studied in this thesis.

Material	ω_{\log} [K]	smearing	Lambda	T_c [K]
$\text{Al}_2\text{Li}_2\text{Pd}_2$	251.285	0.009	0.34	0.15
$\text{Al}_2\text{Li}_3\text{Pd}$	277.663	0.003	0.34	0.17
Al_3LiPd_2	207.417	0.007	0.37	0.27
AlLi_2Pd_3	216.483	0.003	0.13	0.00
AlLi_4Pd	180.642	0.002	0.55	2.43
Al_2LiPd	283.484	0.005	0.27	0.008
AlLiPd_2	233.480	0.002	0.21	0.00
Al_4LiPd	302.472	0.007	0.21	0.00
$\text{Al}_2\text{Li}_2\text{Pd}$	290.365	0.005	0.31	0.059

Table 5.2: Summary of the T_c calculations for the $\text{Al}_x\text{Li}_y\text{Pd}_z$ ternary materials.

Chapter 6

Conclusions

The phonon spectra and densities of states for phonons for most of the materials under study showed groups of normal modes where the acoustic normal modes are dominated by the Palladium contribution. The highest optical frequencies originate from Lithium, the lightest element in all materials. The lower optical frequencies are mostly dominated by Aluminum, which is the second lightest element.

The material with the highest transition temperature is AlLi_4Pd . This material has a larger Li content than the others, which might explain its higher transition temperature. However, the second highest T_c material is Al_3LiPd_2 , with $T_c = 0.27$ K, where the greatest contribution seems to come from Al atoms.

Unfortunately, if we consider the accuracy of the computational methods for conventional superconductors to be 20% [54], these materials may, in practice, not show superconducting properties. But they might present other phenomena with technological applications, like, e.g., mechanical resistivity.

In our work, we didn't proceed with phonon spectra and critical temperature calculation of a few other new metallic materials discovered by members of the research group because they have very low symmetry and that implies high computational cost. This could be the next step of this work, in order to fully explore all metallic ternary materials $\text{Al}_x\text{Li}_y\text{Pd}_z$.

Appendix A

A. The 230 crystallographic space groups

In three-dimensional space there are 230 crystallographic space groups as the next table shows

Table A.1: The 230 Crystallographic Space Groups (adapted from [12])

Crystal System	Laue Class	Crystal Class	Lattice Centring	230 3-Dimensional Space Groups
Triclinic	-1	1 -1	P	P1 P-1
Monoclinic	2/m	2 m 2/m	P C P C P C	P2, P2 ₁ C2 Pm, Pc Cm, Cc P2/m, P2 ₁ m, P2/c, P2 ₁ c C2/m, C2/c
Orthorhombic	mmm	222 mm2 mmm	P C F I P C or A Ama2, Aba2 F I P	P222, P222 ₁ , P2 ₁ 2 ₁ 2, P2 ₁ 2 ₁ 2 ₁ C222, C222 ₁ F222 I222, I212121 Pmm2, Pmc2 ₁ , Pcc2, Pma2, Pca2 ₁ , Pnc2, Pmn2 ₁ , Pba2, Pna2 ₁ , Pnn2 Cmm2, Cmc2 ₁ , Ccc2, Amm2, Abm2, Fmm2, Fdd2 Imm2, Iba2, Ima2 Pmmm, Pnnn, Pccm, Pban, Pmma, Pnna, Pmna, Pcca, Pbam, Pccn,

			C	Pbcm, Pnmm, Pmmn, Pbcn, Pbca, Pnma	
			F	Cmmm, Cmcm, Cmca, Cccm, Cmma, Ccca	
			I	Fmmm, Fddd Immm, Ibam, Ibcm, Imma	
Tetragonal	4/m	4	P	P4, P4 ₁ , P4 ₂ , P4 ₃	
			I	I4, I4 ₁	
		-4	P	P-4	
			I	I-4	
	4/mmm	4/m		P	P4/m, P4 ₂ /m, P4/n, P4 ₂ /n
				I	I4/m, I4 ₁ /a
			422	P	P422, P4 ₂ 12, P4 ₁ 22, P4 ₁ 2 ₁ 2, P4 ₂ 22, P4 ₂ 2 ₁ 2, P4 ₃ 22, P4 ₃ 2 ₁ 2
				I	I422, I4 ₂ 12
		4mm		P	P4mm, P4bm, P4 ₂ cm, P4 ₂ nm, P4cc, P4nc, P4 ₂ mc, P4 ₂ bc
				I	I4mm, I4cm, I4 ₁ md, I4 ₁ cd
			-42m	P	P-42m, P-42c, P-42 ₁ m, P-42 ₁ c
				I	I-42m, I-42d
		-4m2		P	P-4m2, P-4c2, P-4b2, P-4n2
	I		I-4m2, I-4c2		
4/mmm	P		P4/mmm, P4/mcc, P4/nbm, P4/nnc, P4/mbm, P4/mnc, P4/nmm, P4/ncc, P4 ₂ /mmc, P4 ₂ /mcm, P4 ₂ /nbc, P4 ₂ /nnm, P4 ₂ /mbc, P4 ₂ /mcm, P4 ₂ /nmc, P4 ₂ /ncm		
		I	I4/mmm, I4/mcm, I4 ₁ /amd, I4 ₁ /acd		
Trigonal	-3	3	P	P3, P3 ₁ , P3 ₂	
			R	R3	
	-3m	-3		P	P-3
				R	R-3
			312	P	P312, P3 ₁ 12, P3 ₂ 12
				R	R32
		321	P	P321, P3 ₁ 21, P3 ₂ 21	
				R	R32
		31m	P	P31m, P31c	
		3m1	P	P3m1, P3c1	
			R	R3m, R3c	
	P	P-31m, P-31c			
		P	P-3m1, P-3c1		

		R	R-3m, R-3c	
Hexagonal	6/m 6/mmm	6 -6 6/m 622 6mm -6m2 -62m 6/mmm	P	P6, P6 ₁ , P6 ₂ , P6 ₃ , P6 ₄ , P6 ₅ P-6 P6/m, P6 ₃ /m P622, P6 ₁ 22, P6 ₂ 22, P6 ₃ 22, P6 ₄ 22, P6 ₅ 22 P6mm, P6cc, P63cm, P63mc P-6m2, P-6c2 P-62m, P62c P6/mmm, P6/mcc, P6 ₃ /mcm, P6 ₃ /mmc
Cubic	m-3 m-3m	23 m-3 432 -43m m-3m	P F I P F I P F I P F I P F I	P23, P2 ₁ 3 F23 I23, I2 ₁ 3 Pm-3, Pn-3, Pa-3 Fm-3, Fd-3 Im-3, Ia-3 P432, P4 ₂ 32, P4 ₃ 32, P4 ₁ 32 F432, F4 ₁ 32 I432, I4 ₁ 32 P-43m, P-43n F-43m, F-43c I-43m, I-43d Pm-3m, Pn-3n, Pm-3n, Pn-3m Fm-3m, Fm-3m, Fd-3m, Fd-3c Im-3m, Ia-3d
Crystal Sys- tem	Laue Class	Crystal Class	Lattice Centring	230 3-Dimensional Space Groups

Bibliography

- [1] J. Chelikowsky, “Electrons in semiconductors: empirical and ab initio pseudopotential theories,” 2011.
- [2] E. Kaxiras, *Atomic and electronic structure of solids*. 2003.
- [3] S. A. Holgate, *Understanding solid state physics*. cRc Press, 2021.
- [4] T. Biswas, *Study of Extraordinary Light Guidance in Plasmonic Hollow Core Photonic Crystal Fiber (PCF) and in Specialty PCFs at Dirac Point for Emerging Niche Applications*. PhD thesis, University of Calcutta, 2017.
- [5] S. S. Rath, *Comparison of CPFEM and spectral solution methods in prediction of strains near grain boundaries in a uniaxially loaded oligocrystalline tensile specimen*. Michigan State University, 2016.
- [6] W. Setyawan and S. Curtarolo, “High-throughput electronic band structure calculations: Challenges and tools,” *Computational materials science*, vol. 49, no. 2, pp. 299–312, 2010.
- [7] M. Dove, “Introduction to the theory of lattice dynamics,” *École thématique de la Société Française de la Neutronique*, vol. 12, pp. 123–159, 2011.
- [8] M. T. Dove and M. T. Dove, *Structure and dynamics: an atomic view of materials*, vol. 1. Oxford University Press, 2003.
- [9] R. Kar, T. Goswami, B. C. Paul, and A. Misra, “On magnon mediated cooper pair formation in ferromagnetic superconductors,” *AIP Advances*, vol. 4, no. 8, p. 087126, 2014.
- [10] A. Kokalj, “Xcrysden—a new program for displaying crystalline structures and electron densities,” *Journal of Molecular Graphics and Modelling*, vol. 17, no. 3-4, pp. 176–179, 1999.
- [11] P. Coleman, *Introduction to many-body physics*. Cambridge University Press, 2015.
- [12] “The 230 3-dimensional space groups.” <http://pd.chem.ucl.ac.uk/pdnn/symm3/allsgp.htm>. Accessed: 21-09-2022.
- [13] A. V. Narlikar, *Superconductors*. Oxford University Press, 2014.
- [14] P. M. d. C. Borlido, *Atomic ionization energies with hybrid functionals*. PhD thesis, 2014.

- [15] D. Sholl and J. A. Steckel, *Density functional theory: a practical introduction*. John Wiley & Sons, 2011.
- [16] S. Kurth, M. Marques, and E. Gross, “Electronic structure: Density functional theory,” 2003.
- [17] F. Giustino, *Materials modelling using density functional theory: properties and predictions*. Oxford University Press, 2014.
- [18] D. Marx and J. Hutter, *Ab initio molecular dynamics: basic theory and advanced methods*. Cambridge University Press, 2009.
- [19] R. M. Martin, *Electronic structure: basic theory and practical methods*. Cambridge university press, 2020.
- [20] A. Szabo and N. S. Ostlund, *Modern quantum chemistry: introduction to advanced electronic structure theory*. Courier Corporation, 2012.
- [21] E. Engel and R. M. Dreizler, “Density functional theory,” *Theoretical and Mathematical Physics*, pp. 351–399, 2011.
- [22] S. Baroni, S. De Gironcoli, A. Dal Corso, and P. Giannozzi, “Phonons and related crystal properties from density-functional perturbation theory,” *Reviews of modern Physics*, vol. 73, no. 2, p. 515, 2001.
- [23] C. Fiolhais, F. Nogueira, and M. A. Marques, *A primer in density functional theory*, vol. 620. Springer Science & Business Media, 2003.
- [24] P. Schwerdtfeger, “The pseudopotential approximation in electronic structure theory,” *ChemPhysChem*, vol. 12, no. 17, pp. 3143–3155, 2011.
- [25] G. Wang, B. Kincaid, H. Zhou, A. Annaberdiyev, M. C. Bennett, J. T. Krogel, and L. Mitas, “A new generation of effective core potentials from correlated and spin-orbit calculations: selected heavy elements,” *arXiv preprint arXiv:2202.04747*, 2022.
- [26] A. M. Mendez, D. M. Mitnik, and J. E. Miraglia, “Collision processes using effective potentials,” in *Advances in Quantum Chemistry*, vol. 79, pp. 179–200, Elsevier, 2019.
- [27] D. Hamann, M. Schlüter, and C. Chiang, “Norm-conserving pseudopotentials,” *Physical Review Letters*, vol. 43, no. 20, p. 1494, 1979.
- [28] E. L. Shirley, D. C. Allan, R. M. Martin, and J. Joannopoulos, “Extended norm-conserving pseudopotentials,” *Physical Review B*, vol. 40, no. 6, p. 3652, 1989.
- [29] H. Ibach and H. Lüth, *Solid-state physics: an introduction to principles of materials science*. Springer Science & Business Media, 2009.
- [30] S. M. Girvin and K. Yang, *Modern condensed matter physics*. Cambridge University Press, 2019.

- [31] R. K. Puri and V. Babbar, *Solid state physics and electronics*. S. Chand Publishing, 2008.
- [32] N. W. Ashcroft, N. D. Mermin, *et al.*, “Solid state physics,” 1976.
- [33] C. Kittel, “Introduction to solid state physics eighth edition,” 2021.
- [34] J. Singleton, *Band theory and electronic properties of solids*, vol. 2. Oxford University Press, 2001.
- [35] H. J. Monkhorst and J. D. Pack, “Special points for brillouin-zone integrations,” *Physical review B*, vol. 13, no. 12, p. 5188, 1976.
- [36] A. Rose-Innes and E. Rhoderick, “Introduction to superconductivity. pergaman,” 1978.
- [37] G. A. Ummarino, “eliashberg theory. emergent phenomena in correlated matter: Autumn school organized by the forschungszentrum jülich and the german research school for simulation sciences at forschungszentrum jülich 23-27 september 2013,” *Lecture Notes of the Autumn School Correlated Electrons*, vol. 3, p. 2013, 2013.
- [38] F. Marsiglio, “Eliashberg theory: A short review,” *Annals of Physics*, vol. 417, p. 168102, 2020.
- [39] W. McMillan, “Transition temperature of strong-coupled superconductors,” *Physical Review*, vol. 167, no. 2, p. 331, 1968.
- [40] P. B. Allen and R. Dynes, “Transition temperature of strong-coupled superconductors reanalyzed,” *Physical Review B*, vol. 12, no. 3, p. 905, 1975.
- [41] J. Nagamatsu, N. Nakagawa, T. Muranaka, Y. Zenitani, and J. Akimitsu, “Superconductivity at 39 k in magnesium diboride,” *nature*, vol. 410, no. 6824, pp. 63–64, 2001.
- [42] H. J. Choi, D. Roundy, H. Sun, M. L. Cohen, and S. G. Louie, “First-principles calculation of the superconducting transition in mgb 2 within the anisotropic eliashberg formalism,” *Physical Review B*, vol. 66, no. 2, p. 020513, 2002.
- [43] P. Giannozzi, O. Andreussi, T. Brumme, O. Bunau, M. B. Nardelli, M. Calandra, R. Car, C. Cavazzoni, D. Ceresoli, M. Cococcioni, *et al.*, “Advanced capabilities for materials modelling with quantum espresso,” *Journal of physics: Condensed matter*, vol. 29, no. 46, p. 465901, 2017.
- [44] P. Giannozzi, S. Baroni, N. Bonini, M. Calandra, R. Car, C. Cavazzoni, D. Ceresoli, G. L. Chiarotti, M. Cococcioni, I. Dabo, *et al.*, “Quantum espresso: a modular and open-source software project for quantum simulations of materials,” *Journal of physics: Condensed matter*, vol. 21, no. 39, p. 395502, 2009.
- [45] B. G. Pfrommer, M. Côté, S. G. Louie, and M. L. Cohen, “Relaxation of crystals with the quasi-newton method,” *Journal of Computational Physics*, vol. 131, no. 1, pp. 233–240, 1997.

- [46] M. J. van Setten, M. Giantomassi, E. Bousquet, M. J. Verstraete, D. R. Hamann, X. Gonze, and G.-M. Rignanese, “The pseudodojo: Training and grading a 85 element optimized norm-conserving pseudopotential table,” *Computer Physics Communications*, vol. 226, pp. 39–54, 2018.
- [47] J. A. Alarco, P. C. Talbot, and I. D. Mackinnon, “Phonon dispersion models for mgb2 with application of pressure,” *Physica C: Superconductivity and its applications*, vol. 536, pp. 11–17, 2017.
- [48] H. Harima, “Energy band structures of mgb2 and related compounds,” *Physica C: Superconductivity*, vol. 378, pp. 18–24, 2002.
- [49] I. Mazin and V. Antropov, “Electronic structure, electron–phonon coupling, and multiband effects in mgb2,” *Physica C: Superconductivity*, vol. 385, no. 1-2, pp. 49–65, 2003.
- [50] A. Ivanovskii, “Band structure and properties of superconducting mgb2 and related compounds (a review),” *Physics of the Solid State*, vol. 45, no. 10, pp. 1829–1859, 2003.
- [51] Y. Hinuma, G. Pizzi, Y. Kumagai, F. Oba, and I. Tanaka, “Band structure diagram paths based on crystallography,” *Computational Materials Science*, vol. 128, pp. 140–184, 2017.
- [52] T. Williams, C. Kelley, R. Lang, D. Kotz, and J. Campbell, “1 gnuplot,” 2004.
- [53] I. D. Mackinnon, P. C. Talbot, and J. A. Alarco, “Phonon dispersion anomalies and superconductivity in metal substituted mgb2,” *Computational Materials Science*, vol. 130, pp. 191–203, 2017.
- [54] J. A. Flores-Livas, L. Boeri, A. Sanna, G. Profeta, R. Arita, and M. Eremets, “A perspective on conventional high-temperature superconductors at high pressure: Methods and materials,” *Physics Reports*, vol. 856, pp. 1–78, 2020.